Supporting Information

Oriented design of π-conjugated polymer framework for high-performance solid-state lithium batteries

Xian Wu[1,†], Wei Zhang[1,2,†], Haotian Qu[1,†], Chaohong Guan[3], Chuang Li[1], Gongxun Lu[1], Chengshuai Chang[1], Zhoujie Lao[1], Yanfei Zhu[1], Lu Nie[1] and Guangmin Zhou[1,*]

[1] *Shenzhen Geim Graphene Center, Tsinghua-Berkeley Shenzhen Institute & Tsinghua Shenzhen International Graduate School, Tsinghua University, Shenzhen 518055, P. R. China*

[2] *Christopher Ingold Laboratory, Department of Chemistry, University College London, London WC1H 0AJ, UK*

[3] *University of Michigan−Shanghai Jiao Tong University Joint Institute, Shanghai Jiao Tong University, Shanghai 200240, China*

[†] These authors were equal major contributors.

E-mail: guangminzhou@sz.tsinghua.edu.cn

Supplementary Text

Experimental Section

Synthesis of NUS-9 nanosheets and ANFs: NUS-9 nanosheets were synthesized by an interfacial polymerization (IP) approach as previously reported.[1] 0.75 mmol diaminobenzenesulfonic acid (Pa-SO_3H, Aladdin, 99%) was dissolved in 250 mL deionized (DI) water through an ultrasonic treatment as the bottom layer. 0.5 mmol 1,3,5-Triformylphloroglucinol (Tp, 98%) was dissolved in 150 mL octanoic acid (Aladdin, 98%) as the top layer. To control the reaction rate, we added 100 mL of octanoic acid to serve as a buffer layer. The reaction system was kept at room temperature for 5 d under static conditions. Finally, the obtained NUS-9 nanosheets were displayed in DI water for 72 h and gathered by freeze-drying treatment for the next step of preparation and characterization. The ANFs were prepared by proton donor-assisted deprotonation according to the reported literature with some modifications.[2] 4.5g KOH (99%, Aladdin) and 15 mL of DI water were added to 250 mL of DMSO (Aladdin, 99.7%) by stirring at 80 ℃ to obtain a homogeneous solution. 3g PPTA fibers (Dupont) were added to the solution and magnetically stirred at 90 ℃ for 4 h to form ANFs dispersion with a concentration of 15 mg mL^{-1}.

Preparation of the π-conjugated polymer membranes: The NUS-9 and ANFs were mixed to obtain a uniform slurry in mass ratios of 1:*x* (*x* = 0,2,4,8). Then, the slurry was scraped onto a PET substrate and transferred into acetic acid to perform a supramolecular self-assembly process assisted by protonation. Within 2 min, the precursor gel was molded and readily detached from the PET substrate. To completely remove residual solvents, the gel was put into DI water over 12 h and finally dried in air to obtain pure ANF, ACOF-*x* (*x* = 2, 4, 8) membranes.

Preparation of SPE and cathodes:The composite polymer electrolytes for PVHP-COF were prepared through a conventional solution-casting method in a culture dish (diameter: 100 mm) with a PVDF-HFP/LiFSI/NUS-9 weight ratio of 1:1:0.1 using the DMF (Aladdin, 99.8%) solvent. For PANF and PACOF-8, a PVDF-HFP/LiFSI/DMF slurry was first prepared by dissolving 0.3 g PVDF-HFP (M_w=130,000, Macklin) and

0.3 g LiFSI in 3 mL DMF under stirring at 80 ℃. The ANF and ACOF-8 membranes were then immersed in the slurry and allowed to settle until filled by it. At last, the solid-state PVHP-COF, PANF, and PACOF-8 were obtained by drying for 24 h at 60 °C. The cathode was prepared by mixing sulfurized polyacrylonitrile (SPAN, 50.2 wt% of S content), CNT (Macklin), PVDF-HFP, and LiFSI in a weight ratio of 75:15:30:30 (0.75 g:0.15 g:0.3 g:0.3 g) in DMF, followed by casting the slurry on an Al foil. After drying at 60 °C for 12 h, the cathode was prepared with SPAN mass loading of around 1-2 mg cm^{-2}.

Materials characterization: The crystal structures of samples were analyzed with an X-ray diffractometer (Bruker D8 Advance) using Cu-Kα radiation. Morphological and structural analyses were performed by scanning electron microscope (SEM, HITACHI SU8010) with energy dispersive spectroscopy (EDS) and field emission transmission electron microscope (FEI Tecnai F30, 300 kV). X-ray photoelectron spectroscopy (XPS) measurements were conducted by Thermo Scientific K-Alpha. The binding energy of peaks was cailibrated based on C 1s (284.8 eV) referred to the National Institute of Standards and Technology (NIST, USA) database. Raman spectra were obtained with Horiba LabRAM HR800. Fourier transform infrared (FTIR) spectroscopy of the membranes and COFNs was performed with a VERTEX 70 using the attenuated total reflection (ATR) infrared mode. Prior to temperature-dependent FTIR measurements, the samples were Bruker TENSOR Il and the temperature interval was controlled as 20 °C in the temperature range of 30–110 °C. All the temperature-dependent FTIR data were collected to generate 2D correlation spectra in the presetting wavelength ranges using the software 2D Correlation Spectroscopy Analysis. Thermogravimetric analysis (TGA) was performed using Netzsch STA 449F3 thermal analyzer from room temperature to 800 °Cat a heating rate of 10 °C min^{-1} under nitrogen. Thermogravimetry-Fourier transform infrared spectroscopy (TG-FTIR) analysis was carried out in the N_2 atmosphere from 30 to 800 °C at a heating rate of 10 °C min^{-1} by using a NETZSCH TG 209 F1 Libra thermal analyzer. Two-dimensional synchrotron radiation grazing incidence wide-angle X-ray scattering (2D-GIWAXS) was performed at Taiwan Light Source Beamline with a wavelength of 1.027 nm to analyze the

orientation of ACOF-8 membranes. The Small- and wide-angle X-ray scattering (SWAXS) data was measured on XENOCS Nano-inXider. The thickness of COF nanosheets was analyzed by atomic force microscopy (AFM) using Bruker Dimension Icon. POM images were obtained by a Laite LP100 device. The static contact angle between DMF and conjugated polymer membranes was measured by POWEREACH JC2000D. The ^{13}C, ^{7}Li nuclear magnetic resonance (NMR) was performed with a JNM-ECZ600R spectrometer. Zeta potential values were obtained by an Anton-Paar SurPASS 3 instrument. The time-off light secondary ion mass spectrometry (ToF-SIMS) for SEI analysis was conducted after cycling Li||SPAN full cells 20 times at 30 ℃. To assess the DMF capture ability of COFs, quartz crystal microbalance (QCM) measurements were carried out using QSense Analyzer supplied by Biolin Scientific Company.

Electrochemical characterization: All CR2032-type coin cells were assembled in a glove box filled with argon (H_2O < 0.1 ppm, O_2 < 0.1 ppm).

The Li^+ ionic conductivities of the polymer electrolytes were measured by electrochemical impedance spectroscopy measurements, which were performed on an electrochemical analyzer (Bio-logic VMP-300). Prior to conducting the conductivity measurements, the coin cells, configured as SS|SPE|SS, were subjected to a 2-hour thermal equilibration period at each test temperature ranging from 25 to 80 °C in a climate chamber. The ionic conductivity (σ) was calculated according to the following equation (1):

$$\sigma = \frac{L}{S \cdot R} \qquad (1)$$

where *L (cm)* represents the thickness of the polymer electrolyte, *S (cm^{-2})* symbolizes the contact area between stainless-steel and electrolyte, *R (Ω)* is the bulk ohmic resistance obtained by EIS.

The Arrhenius equation was used to fit the ionic conductivities of SPE to calculate the activation energy (E_a):

$$\sigma T = \sigma_0 \exp\left(-E_a / k_B T\right) \qquad (2)$$

where σ (S cm^{-1}) is ionic conductivity, σ_0 symbolizes the pre-exponential factor, T (K)

is absolute temperature, k_B (J K^{-1}) is the Boltzmann constant.

The lithium-ion transference number (t_{Li+}) of the polymer electrolyte was determined through a combination of AC impedance and DC polarization techniques employing a Li|SPE|Li configuration. EIS measurements were conducted both before and after polarization at the open circuit potential, utilizing a perturbation signal of 10 mV within the frequency range of 0.01 to 1 MHz, following the same procedure as the ionic conductivity test. t_{Li+} was calculated according to the following equation (3):

$$t_{\mathrm{Li}^+} = \frac{I_S Rb_S(\Delta V - I_O R_O)}{I_O Rb_O(\Delta V - I_S R_S)} \quad (3)$$

where ΔV denotes the applied polarization voltage of 10 mV; I_o and I_s represent the current before and after polarization; R_o and R_s stand for the initial and final impedance of the polarization process, respectively; and Rb_o and Rb_s are the initial and final resistances of the electrolyte.

LSV was conducted with Li|SPE|SS cells operated in a voltage range from open circuit potential to 6 V under a sweep rate of 0.2 mV s^{-1} at 25 ± 1 °C.

The interfacial characteristics of the polymer electrolyte and lithium anode were detected by assembling coin cells in the configuration of Li|SPE|Li and Li|SPE|Cu, which were tested under different current densities at 30 ℃ without additional pressure.

The galvanostatic cycling was performed with a Li|SPE|SPAN cell under various current rates over a voltage of 1.0-3.0 V (vs. Li^+/Li). The temperature of testing was 30 ℃ in a climate chamber.

Computational methods

MD simulations: MD simulations were conducted to gain the distribution of solvated molecules in the channels of COF. Firstly, the molecular structures of DMF and LiFSI were optimized by the Gaussian software[3] based on the density functional theory (DFT) method with the B3LYP and 6-31+G(d,p) basis set. Then the COF nanosheet, LiFSI, and DMF molecules were in the supercell with 40×46×17 $Å^3$. The system was modeled by Large Scale Atomic/Molecular Massively Parallel Simulator code[4] with PCFF, NVT (constant particle number, volume, and temperature). The electric field was applied for simulation along the Z direction with the value of 0.5 V $Å^{-1}$. The initial velocities were

random, and the Andersen thermostat was employed to maintain a constant simulation temperature of 298.0 K. The time step was set as 2 fs, and the total simulation time of each model was 4 ns. For the PVHP/DMF/LiFSI system, the equilibration procedure was conducted in an NPT ensemble. In addition, we attained theoretical insights into the DMF solvent capture by NUS-9 channels through MD simulations.

DFT calculations: Periodic DFT calculations containing geometry optimizations of NUS-9 and ANF crystals were performed within the CP2K program package.[5] The unit cells of NUS-9 and ANF were both expanded into supercells with a = 15.74 Å, b = 15.54 Å, c = 25.8 Å and a = 22.8345 Å, b = 22.9439 Å, c = 20.6232 Å for geometry optimizations, respectively. The electronic structures of the optimized structures were then computed using the wB97M-V exchange-correlation density functional within Gaussian and Augmented Plane Wave Method (GAPW).[6-8]

In order to visualize the bonding arrangements and weak interactions among internal atoms in the crystals, we used the interaction region indicator (IRI).[9] The IRI method quantifies the electron density and its gradient generated by DFT calculations, allowing it to reveal both chemical bonds and weak interactions in chemical systems for drawing the corresponding 3D isosurface representations. The Multiwfn program[10] was used for IRI analyses and the VMD program[11] was used for visualization.

The geometries of the units of NUS-9 and ANF were fully optimized by means of ωB97X-D/6-311(d,p) within the Gaussian 09 suite of programs[3], and the frontier orbital levels and isosurfaces were obtained at the same level. To investigate the delocalization of π electrons featured by π-conjugated polymers, the wavefunction analysis code Multiwfn was used to identify the type of localized molecular orbitals (LMOs) and performed a π electronic structure analysis.[12] Additionally, we conducted potential energy scan (PES) to evaluate the rigid of π-conjugated polymers based on ωB97X-D/6-311G(d, p).[13]

The independent gradient model based on Hirshfeld partition (IGMH) was then applied to visualize the noncovalent interactions between the ANF monomer and the COF fragment within the Multiwfn program.[14] The geometries of the complexes were fully optimized without symmetry or geometry constraint based on r2SCAN-3c/def2-

TZVP, which were performed with the ORCA program system-Version 5.0.[15, 16]

COMSOL Multiphysics simulations: We employed the finite-element method using the COMSOL Multiphysics 6.2 platform[17], combining the Lithium-ion Battery module, the Transport of Diluted Species module, the Deformed Geometry module, and the Level Set module to complete the simulation process.

The model domain was divided into lithium metal phase, SPEs phase, and the contact loss domains. Intricate processes encompassed electron conduction, Li-ion transport, active reactions at the electrode-electrolyte interface, and corresponding side reactions following SEI evolution.

Mass Transport

For the transport of different ions in the liquid phase, it is controlled by the migration induced by electric field and the diffusion controlled by the concentration gradient, which can be expressed by the Nernst-Planck equation:

$$N_{i,m} = -D_{i,m}(\nabla C_i^b + \frac{z_i F C_i^b}{RT}\nabla \Phi_e) \qquad (4)$$

where $D_{i,m}$ is the diffusion coefficient of species i ($i = Li^+$, and A^-, which is the anion of the lithium salt used in the electrolyte) and the index m corresponds to each domain. $N_{i,m}$ is ions flux, C_i^b is the concentration of species i in the electrolyte, z_i is the charge number of species i, F is the Faraday's constant, R is the ideal gas constant, T is the Kelvin temperature and Φ_e is the electrolyte potential.

Charge transfer

At the electrode, lithium ions undergo direct precipitation, forming metallic lithium. The (de)lithiation process can be described by the following reactions, respectively:

$$Li^+ + e^- \underset{d}{\overset{c}{\rightleftharpoons}} Li \qquad (5)$$

The charge transfer rate of the electrochemical reaction can be expressed through the local current density. By assuming the plating reaction to be fully irreversible, Butler-Volmer kinetics can be used to describe the rate of the plating reaction, For each reaction, the current density (j) is determined by the Butler-Volmer equation:

$$j = j_{ex}[\exp(\frac{\alpha_{a,j} F \eta_j}{RT}) - \exp(-\frac{\alpha_{c,j} F \eta_j}{RT})] \qquad (6)$$

here $\alpha_{a,j}$ and $\alpha_{c,j}$ are the anodic and cathodic charge transfer coefficients, respectively, and $j_{ex}$is exchange current density, $\eta_j$is overpotential, which can be calculated from:

$$\eta = \Phi_s - \Phi_e - U_{eq} \quad (7)$$

where Φ_s is the solid phase potential, U_{eq} is the equilibrium potential of the battery.

The exchange current density (j_{ex}) is closely related to the electron transfer kinetics and the concentration gradient near the surface:

$$j_{ex} = j_e \prod_{i,v_j>0} \left(\frac{c_i}{c_{b,i}}\right)^{\alpha_i v_j/n_j} \prod_{i,v_j<0} \left(\frac{c_i}{c_{b,i}}\right)^{*\alpha_i v_j/n_j} \quad (8)$$

where c_i and $c_{b,i}$ are the concentration of each species i near the electrode and in the bulk electrolyte, respectively, j_e is the current density for charge transfer, v_j is the stoichiometric coefficients, n_j is the number of electrons transferred.

Lithium electrode corrosion

The Deformed Geometry module was used to study the morphology evolution of lithium anodes. The rate of side reactions on the anode surface affects the final deposition morphology, and the velocity in the normal direction is defined as:

$$v_n = \frac{FN_{Li^+}}{nF}\frac{M}{\rho} \quad (9)$$

Thus, the morphology of the lithium electrode is determined by the velocity in the normal direction near the surface:

$$v_n = n \cdot \frac{dy}{dt} \quad (10)$$

Where *n* is the normal vector at the lithium electrode surface.

SEI evolution

The Level Set interface is used to keep track of the deformation due to corrosion product deposition. The Level Set interface automatically sets up the equations for the movement of the interface between the PANF and the electrode. The interface is represented by the 0.5 contour of the level set variable ϕ. The level set variable varies from 1 in the electrolyte domain to 0 in the deposited region. The transport of the level set variable is given by:

$$\frac{\partial \phi}{\partial t} + u \cdot \nabla \phi = \gamma \nabla \cdot \left(\varepsilon \nabla \phi - \phi(1-\phi)\frac{\nabla \phi}{|\nabla \phi|}\right) \quad (11)$$

Where the ε parameter determines the thickness of the interface and is defined as

$\varepsilon = h_{max}/4$ where h_{max} is the maximum mesh element size in the domain. The γ parameter determines the amount of reinitialization. A suitable value for γ is the maximum velocity magnitude occurring in the model.

Supplementary Figures

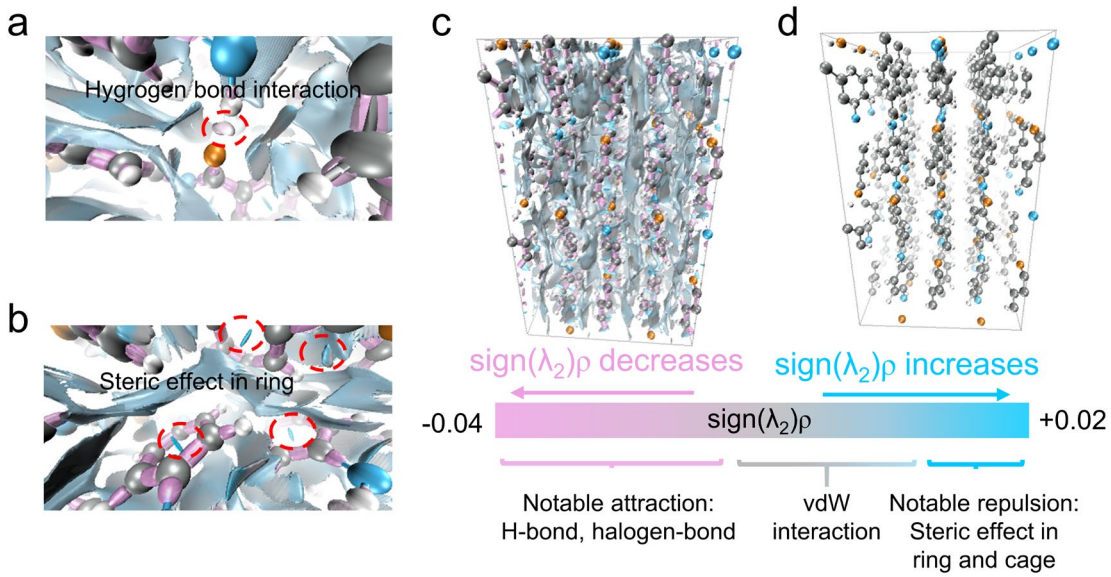

Figure S1. Interaction region indicator (IRI) analysis was induced for visualizing covalent and interactions in an equal footing[18]. Essentially, IRI is the gradient norm of electron density weighted by scaled electron density. The sign(λ_2)ρ function was applied to map on IRI isosurfaces in various colors to distinguish attractive and repulsive interactions, represented as the hydrogen bond (a) and steric effect in the ring (b). High value of ρ devotes to large magnitude of sign(λ2)ρ, which implies a relatively strong attraction and repulsion combined with $\lambda_2 < 0$ or $\lambda_2 > 0$ respectively. While low low ρ and thus small sign(λ2)ρ can be most attributed weak interatomic vdW interaction. In addition, ANF supercell was represented on a 3D view in (c) and (d), and strong hydrogen bonds (C=O…H-N) existed between every two polymer chains.

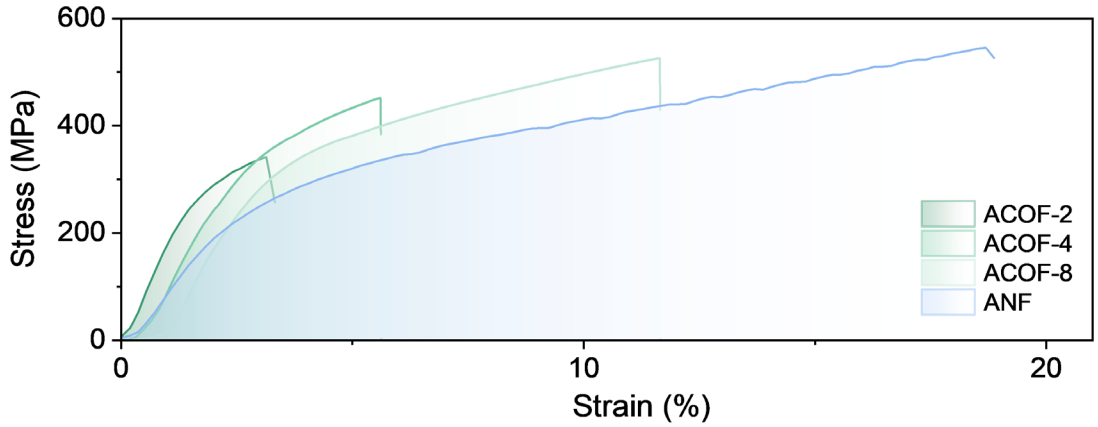

Figure S2. Stress–strain curve of ANF, ACOF-2, ACOF-4, ACOF-8 membranes. They can endure a tensile strength of 544.68 MPa, 339.61 MPa, 450.18 MPa, 525.36 MPa, respectively.

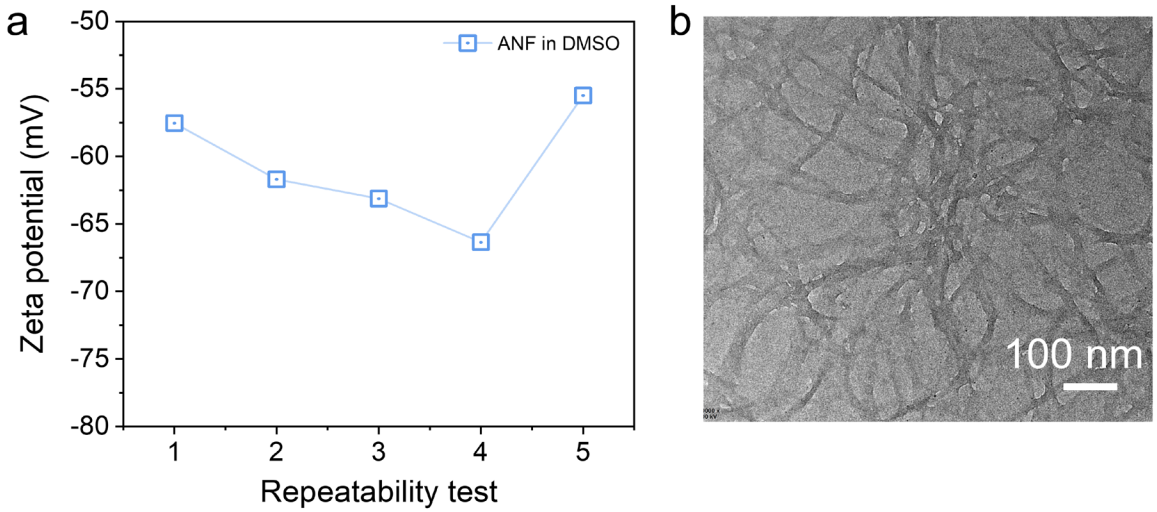

Figure S3. a, Zeta potentials of ANFs dispersion at repeatability test of 1-5. **b**, TEM image of ANFs.

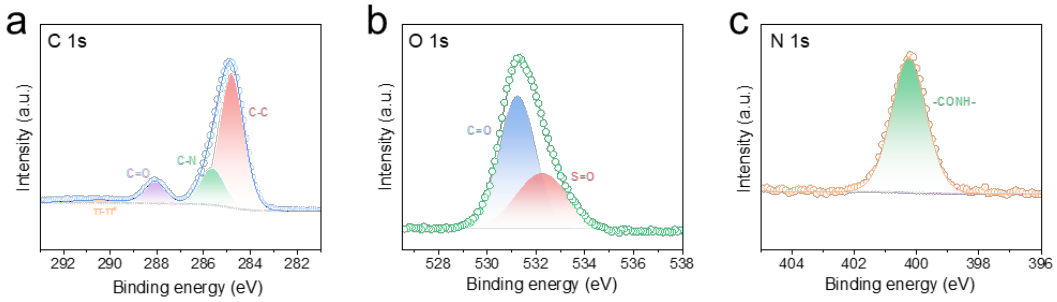

Figure S4. High-resolution XPS of C 1*s* speak (**a**), O 1*s* speak (**b**) and N 1*s* speak (**c**) for pure ANF membrane.

Note: All the spectra are referenced to the C 1*s* peak with 284.8 eV. Besides the main peak at 284.8 eV for C–C and 285.7 eV for C–N, the peak at 288.1 eV was corresponding to the C═O. The π–π interactions of aromatic phenyl groups were demonstrated by the presence of a peak at 290.4 eV[19].

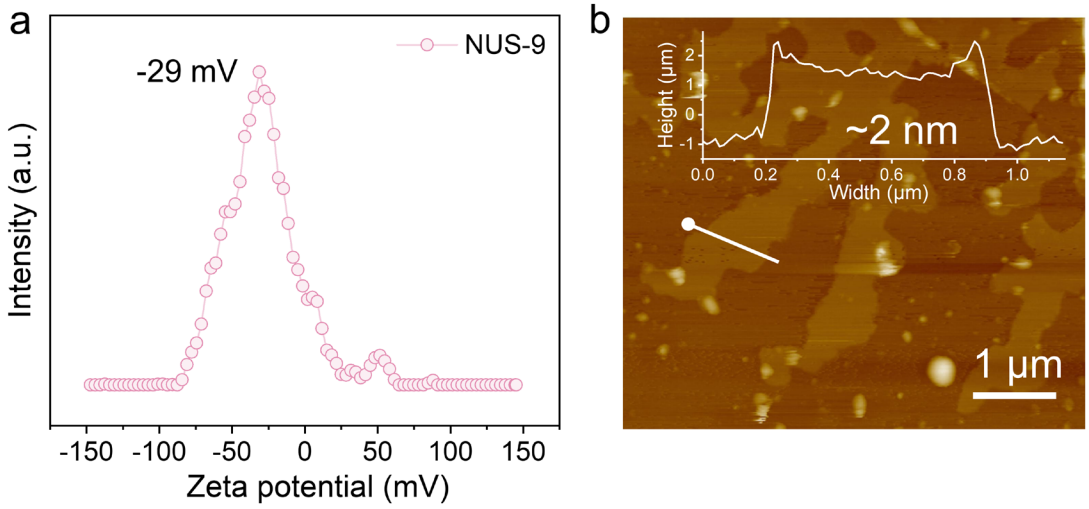

Figure S5. a, Zeta potential of NUS-9 nanosheets aqueous solution. b, AFM image and height profile of NUS-9 nanosheets.

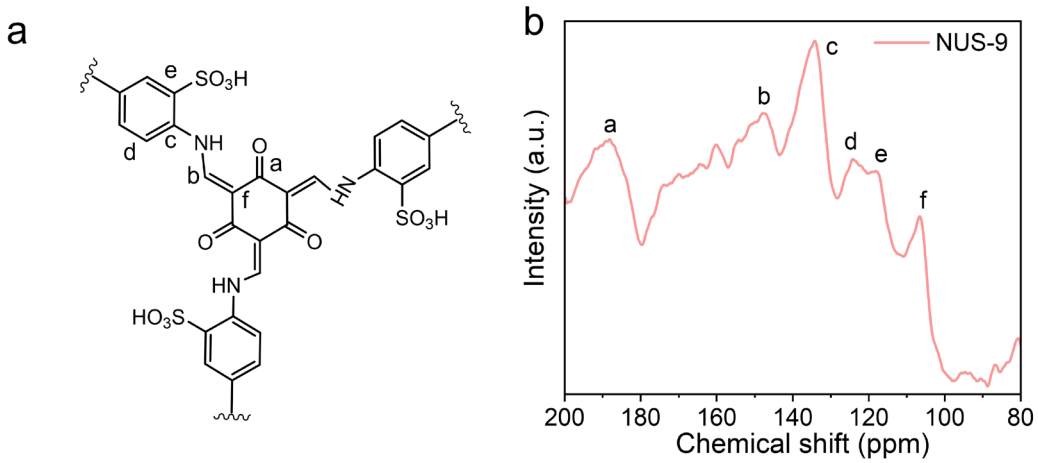

Figure S6. ^{13}C CP-MAS solid-state NMR spectrum of the NUS-9 nanosheets.

Note: The presence of a chemical shift at 187 ppm, indicative of keto carbon (-C=O), verifies the enol-to-keto tautomerization in NUS-9. The chemical shift at 147 ppm was assigned to C=C carbon attached to the N atom. The peaks lay in 147 to 117 ppm were associated with benzene ring[1].

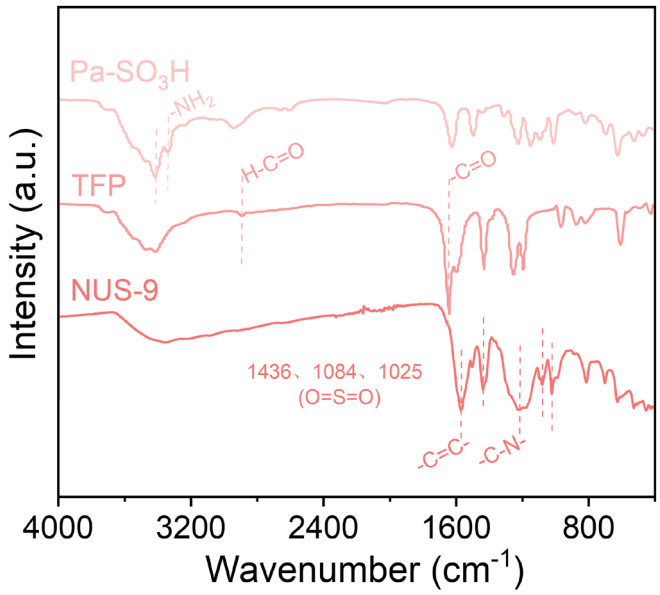

Figure S7. FTIR spectra of Tp, Pa-SO3H, and NUS-9 nanosheets.

Note: The absence of N-H (3420-3340 cm^{-1}) and –C=O (1640 cm^{-1}) stretching bands can be attributed to the complete consumption of aldehyde and diamine monomers in the formed skeletons. Additionally, the signals at 1571 cm^{-1} and 1226 cm^{-1} in the spectrum were assigned to C=C groups and C-N groups, respectively, which further verified the keto-tautomer structure of NUS-9 nanosheets.

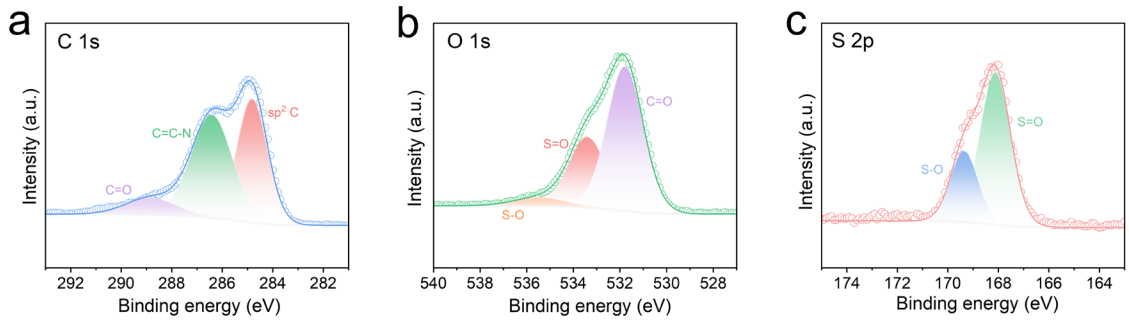

Figure S8. High-resolution XPS of C 1*s* speak (**a**), O 1*s* speak (**b**) and S 2*p* speak (**c**) for NUS-9 nanosheets.

Note: All the spectra are referenced to the C 1s peak with a binding energy of 284.8 eV. The appearance of the S 2*p* peak in XPS spectra of ACOF-8 membrane confirmed the existence of the sulfonic acid groups on NUS-9 skeleton. In the high-resolution C1*s* patterns, the presence of C=C-N and C=O also demonstrates the formation of β-ketoenamine connections. Hence, the above results indicated the successful preparation of NUS-9 nanosheets[20].

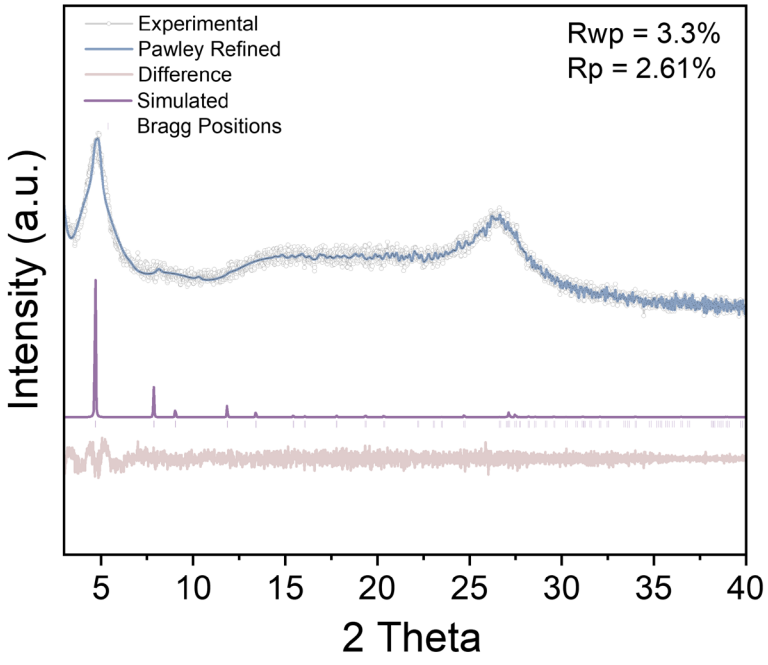

Figure S9. Simulated and experimental powder patterns for NUS-9. The structure model was built using Materials Studio and refined using experimental XRD data.

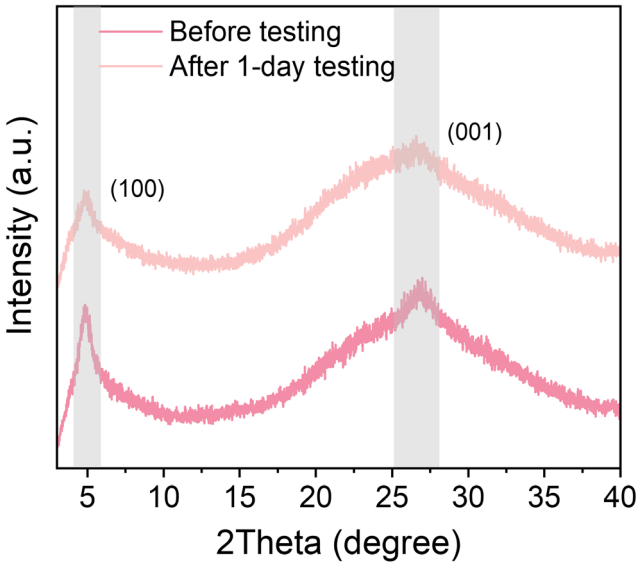

Figure S10. XRD patterns of NUS-9 after the alkali resistance test.

Note: The XRD patterns show that after treatment with 7M KOH, the characteristic peaks of (100) and (001) planes showed no variation, which was attributed to its outstanding chemical stability.

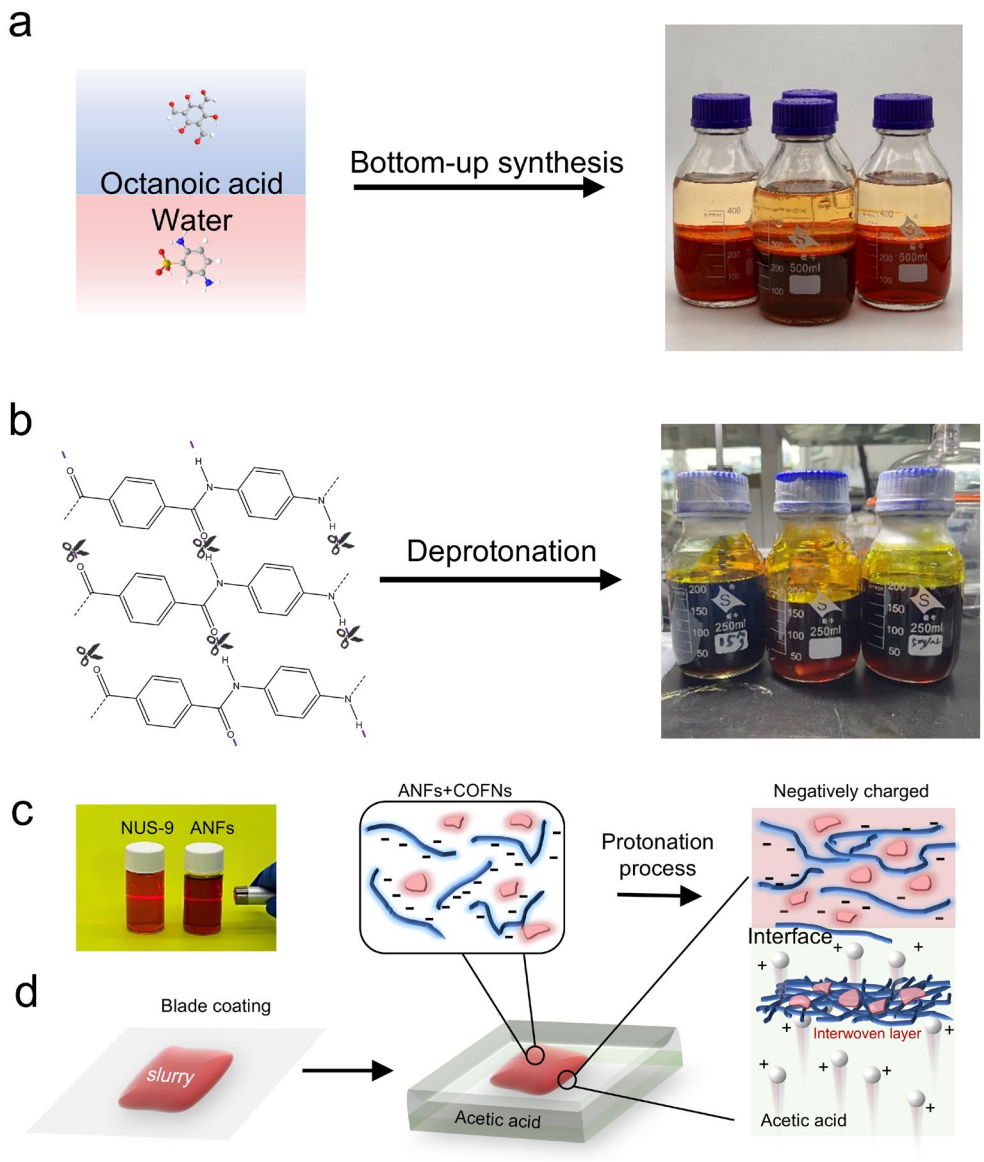

Figure S11. Scheme of preparing NUS-9 nanosheets (**a**) and ANFs (**b**) via bottom-up synthesis and proton donor-assisted deprotonation. **c**, Tyndall effects in the colloidal solutions of NUS-9 nanosheets and ANFs. **d**, Scheme illustrating the self-assembly process of ACOF-x (x=2, 4, 8) membranes.

Note: The well-mixed slurry of ANFs and COFNs is blade-coated onto a substrate and then transferred onto the surface of an acetic acid solution. At this point, protons from the acetic acid rapidly diffuse into the slurry, neutralizing the deprotonated, negatively charged ANFs. The reprotonated ANFs and COFNs form a multilayer interwoven structure through strong hydrogen bonding and π-π stacking interactions, ultimately resulting in the formation of oriented membranes.

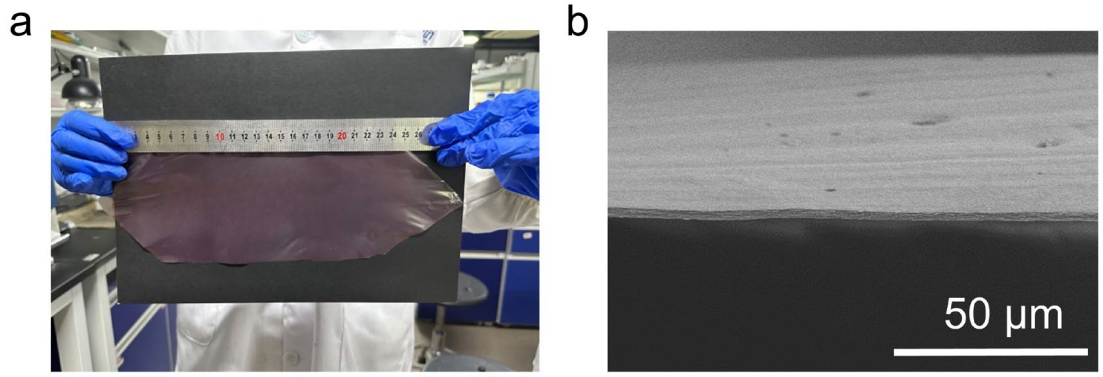

Figure S12. The optical photograph (**a**) and cross-sectional SEM image (**b**) of large-size ACOF-8 membrane.

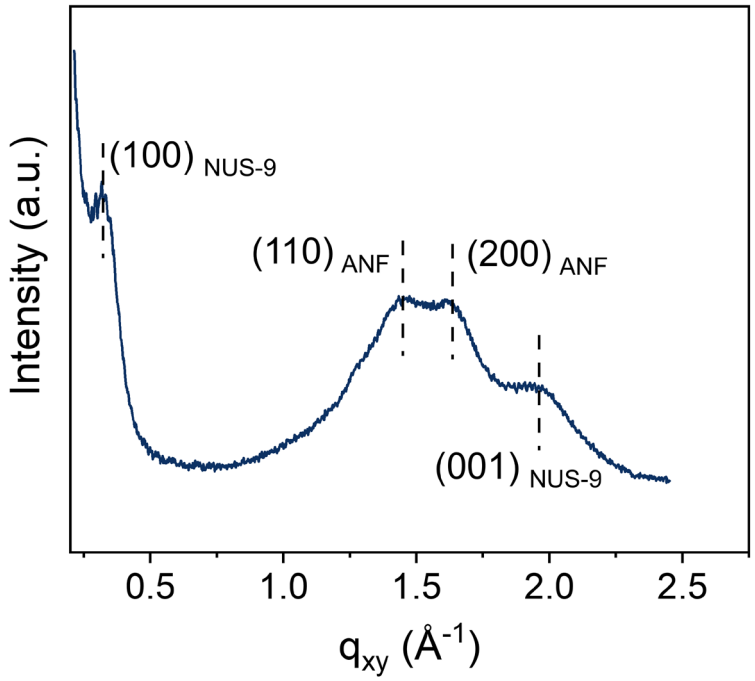

Figure S13. SWAXS profile of ACOF-8 membrane.

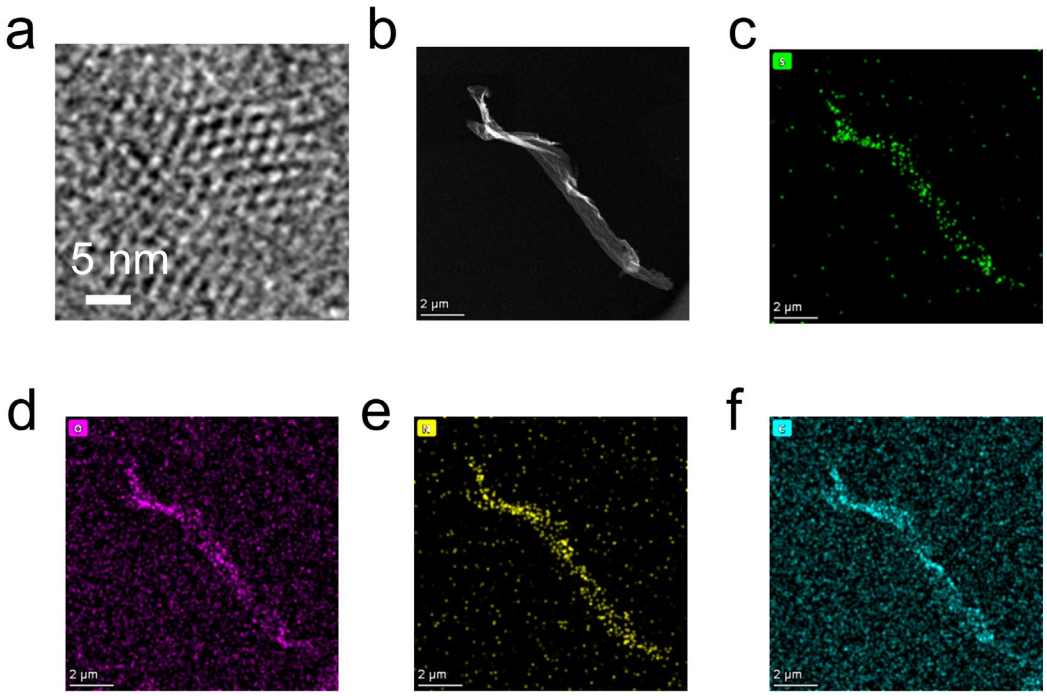

Figure S14. **a**, HRTEM images of NUS-9. **b**, HAADF-STEM image of NUS-9 nanosheet and corresponding EDS elemental distribution map of (**c**) S, (**d**) O, (**e**) N, (**f**) C.

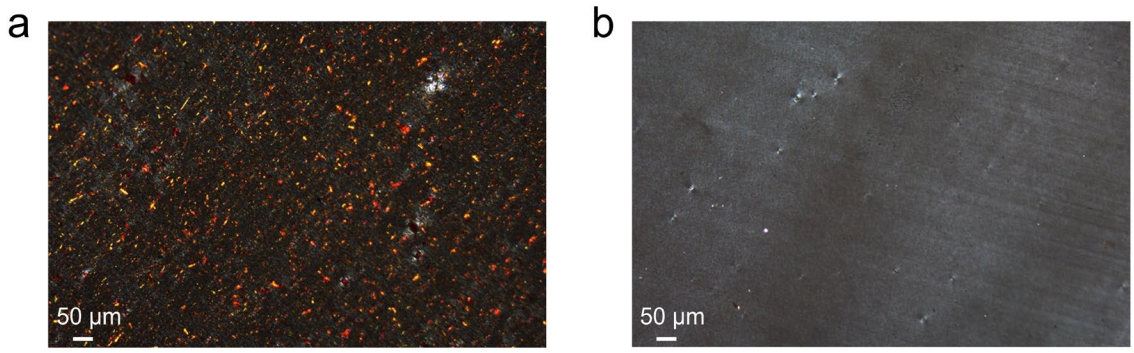

Figure S15. POM images of ACOF-8 (**a**) and ANF (**b**) membrane.

Note: In the orthogonal detection position, the field of view for ANF membrane appeared dark, attributable to its isotropic properties. NUS-9 nanosheets embedded in the ACOF-8 membrane exhibited birefringent properties, leading to a uniformly distributed array of vivid red spots across its surface.

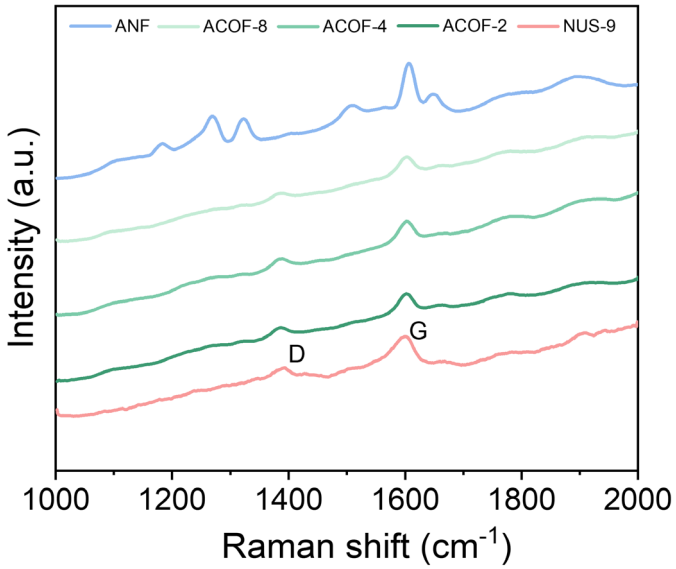

Figure S16. Raman spectroscopy of ANF, NUS-9 and ACOF-x (x=2, 4, 8) membrane.

Note: Raman spectroscopy measurements were performed to identify the composition of π-conjugated membranes. As a characteristic example of imine COFs, NUS-9 exhibited two principal Raman modes: the D mode, corresponding to the vibration of sp^3-hybridized amorphous carbon atoms, and the G mode, associated with the in-plane stretching of sp^2-hybridized carbon atoms[21]. For the ACOF-x (x=2, 4, 8) membranes, Raman spectroscopic analysis of the surface consistently revealed distinct signals at 1384 cm^{-1} and 1601 cm^{-1}, attributable to the NUS-9 component.

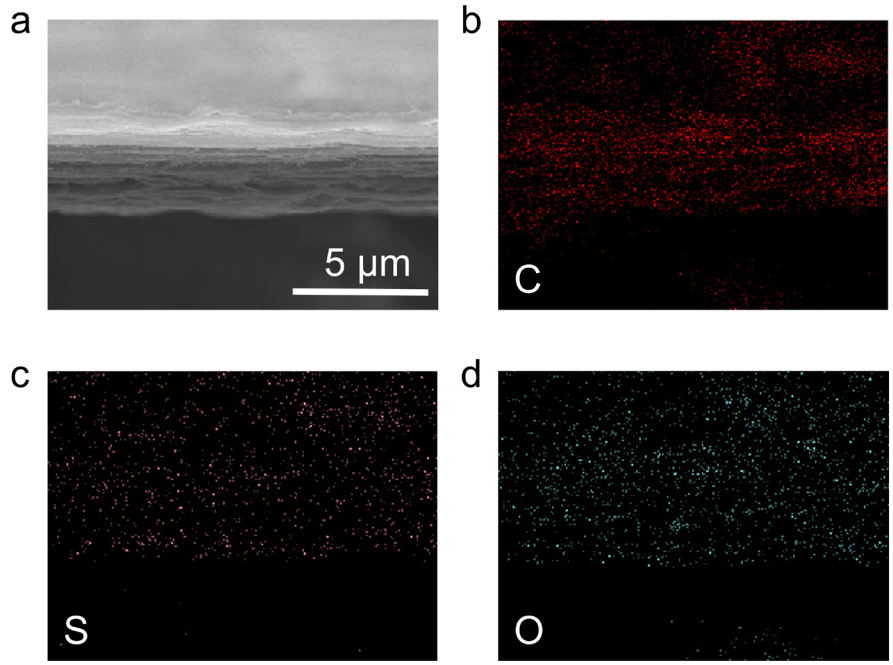

Figure S17. Cross-sectional SEM image (**a**) and EDS mapping results (**b**, **c**, **d**) of ACOF-8 membrane.

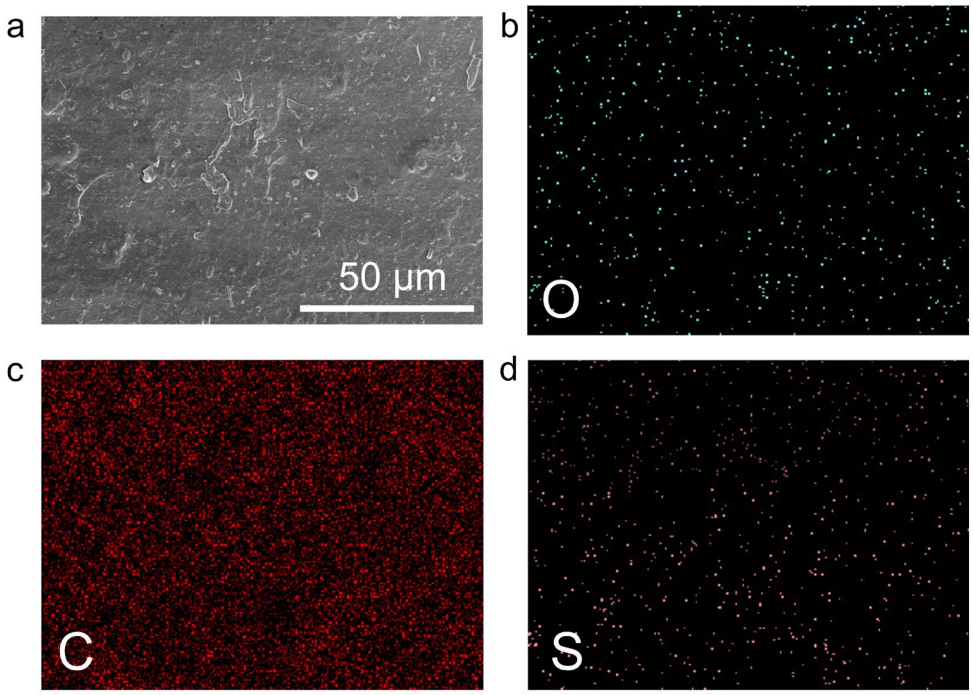

Figure S18. Surface SEM image (**a**) and EDS mapping images (**b**, **c**, **d**) of ACOF-8 membrane.

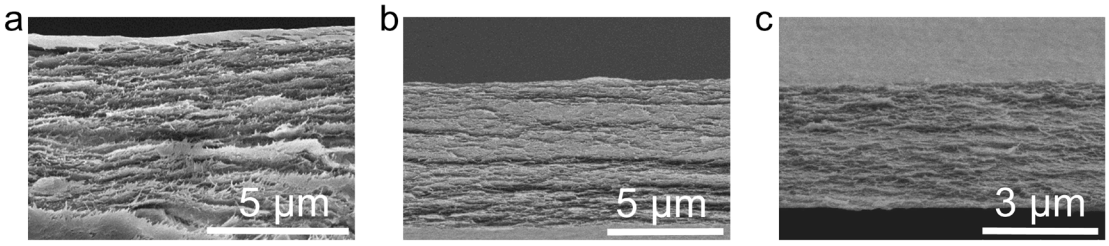

Figure S19. Cross-sectional SEM images of ANF (**a**), ACOF-4 (**b**), ACOF-2 (**c**) membranes.

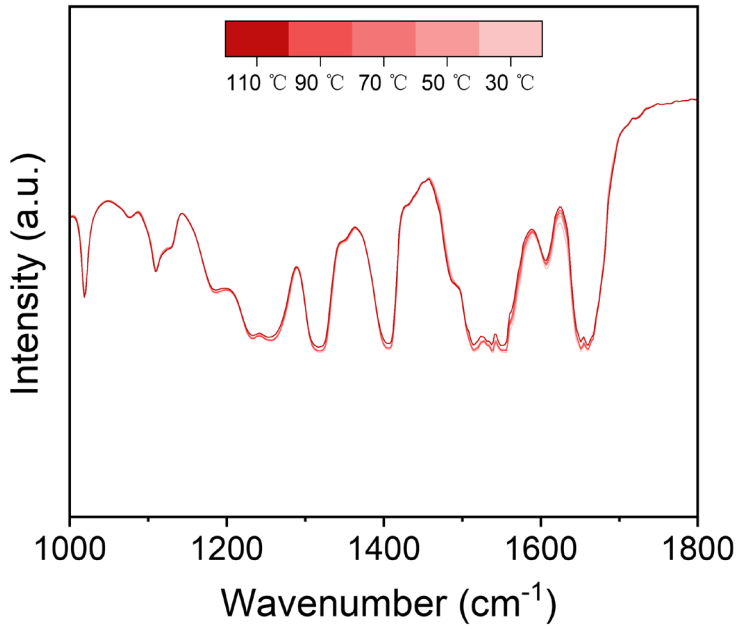

Figure S20. Temperature-variable FTIR spectra of ACOF-8 membrane upon heating from 30 to 110 °C (interval:20 °C).

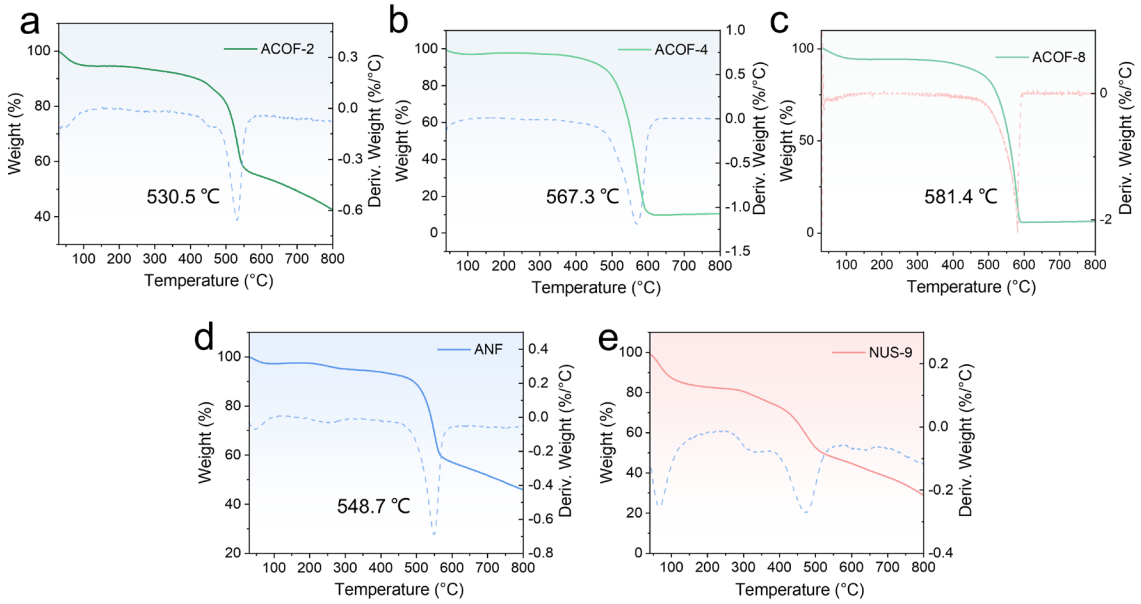

Figure S21. TG and DTA curves of ACOF-2 (**a**), ACOF-4 (**b**), ACOF-8 (**c**), ANF (**d**), NUS-9 (**e**) membranes.

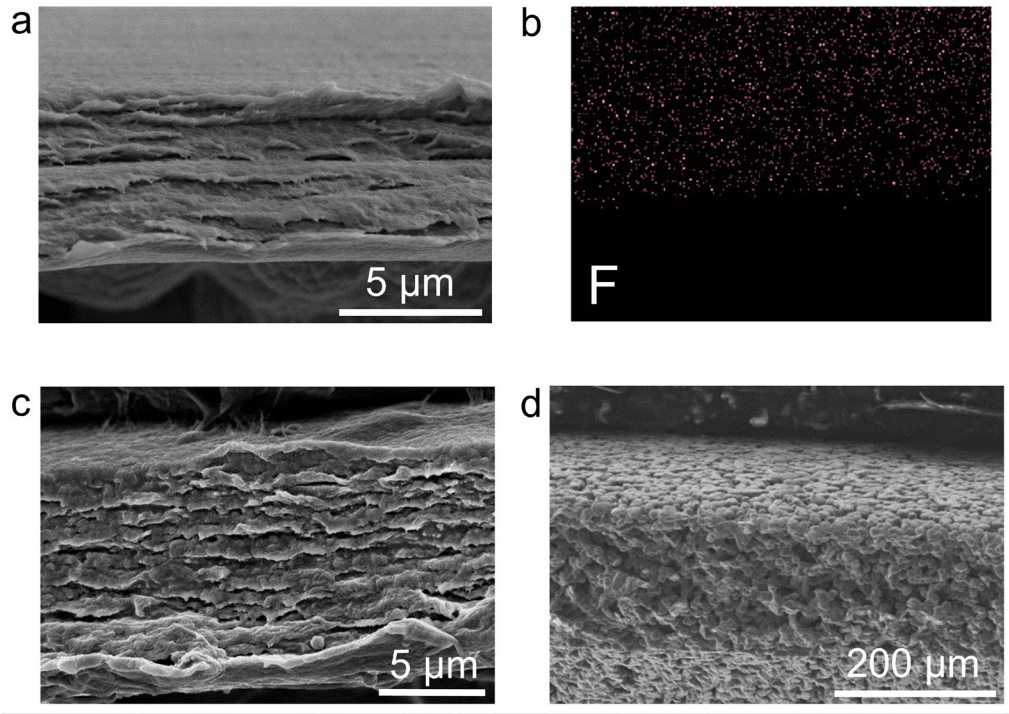

Figure S22. Cross-sectional SEM images of PACOF-8 (**a**) electrolyte and EDS elemental distribution map of (**b**) F. Cross-sectional SEM images of PANF (**c**), PVHP-COF (**d**) electrolytes.

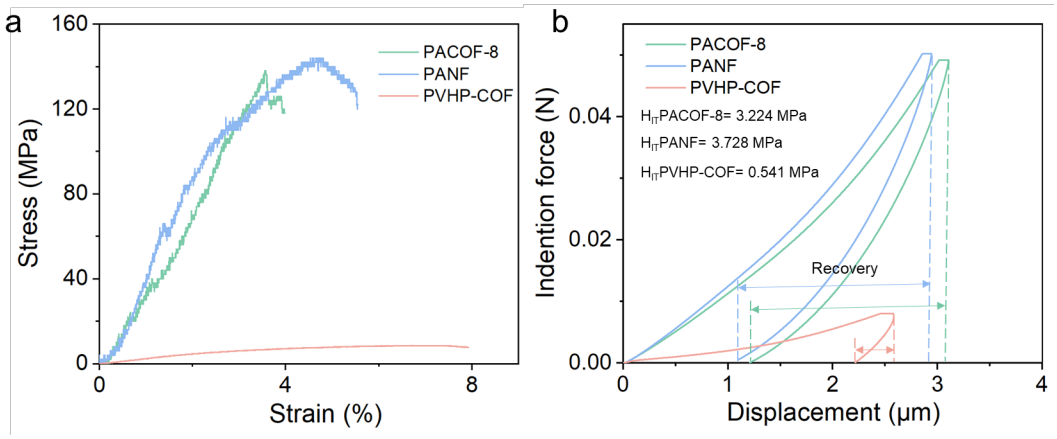

Figure S23. Nanoindentation test (**a**) and stress–strain curve (**b**) of PACOF-8, PANF, PVHP-COF electrolytes.

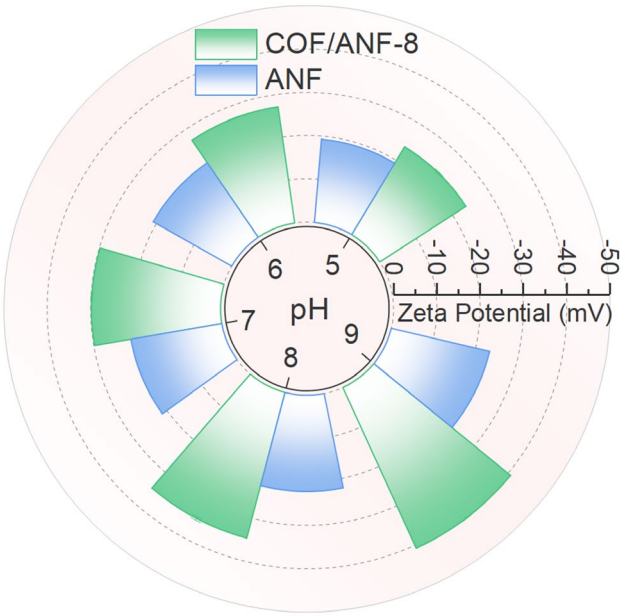

Figure S24. Zeta potential measurements of ACOF-8 and ANF membranes operated under pH of 5,6,7,8,9.

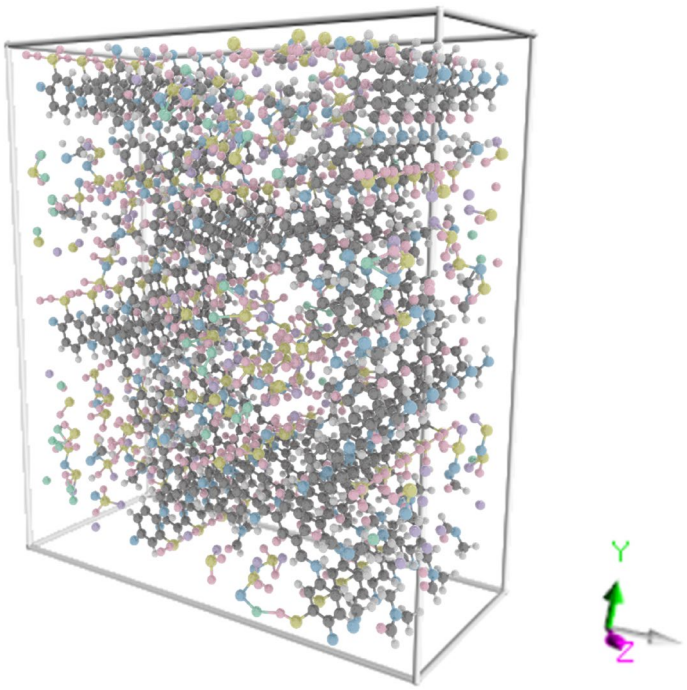

Figure S25. Snapshot of MD simulation for COF/LiFSI/DMF systems (t=0 ps). Color scheme: Li^+ ions, green; O atoms, pink; C atoms, gray; H atoms, white; N atoms, blue; F atoms, purple; S atoms, yellow. For clarity, all are shown in ball-and-stick format.

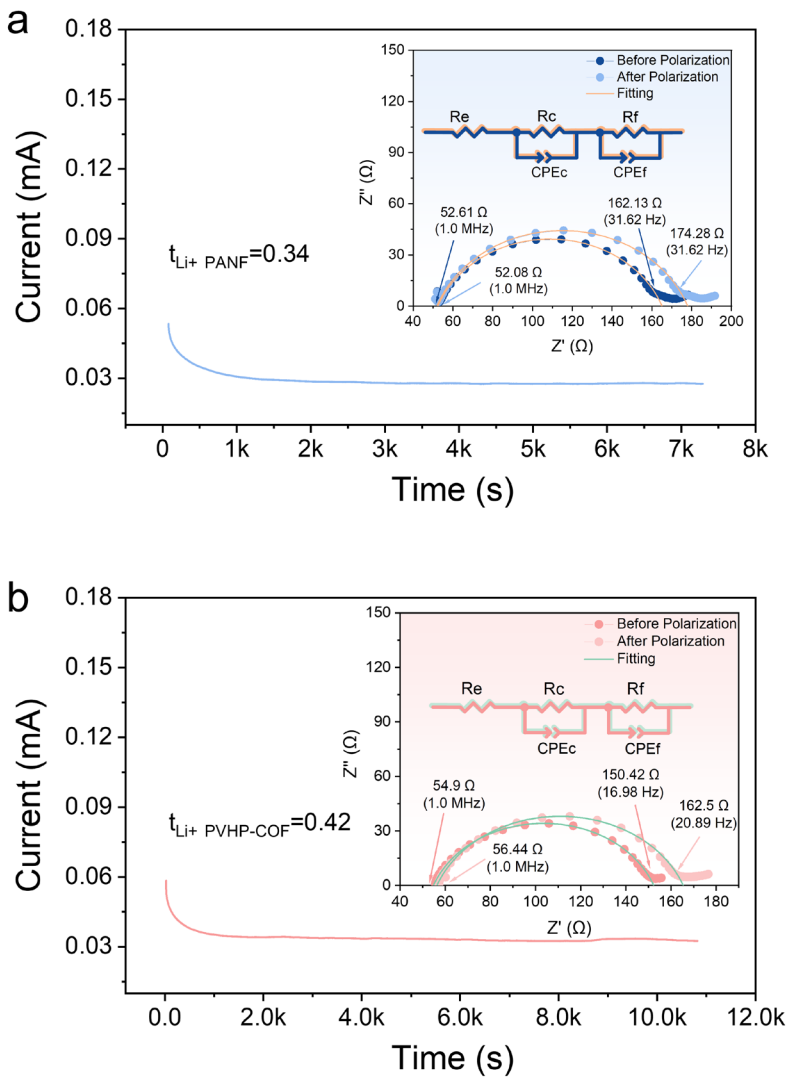

Figure S26. Transference number of PANF (**a**) and PVHP-COF (**b**) electrolytes

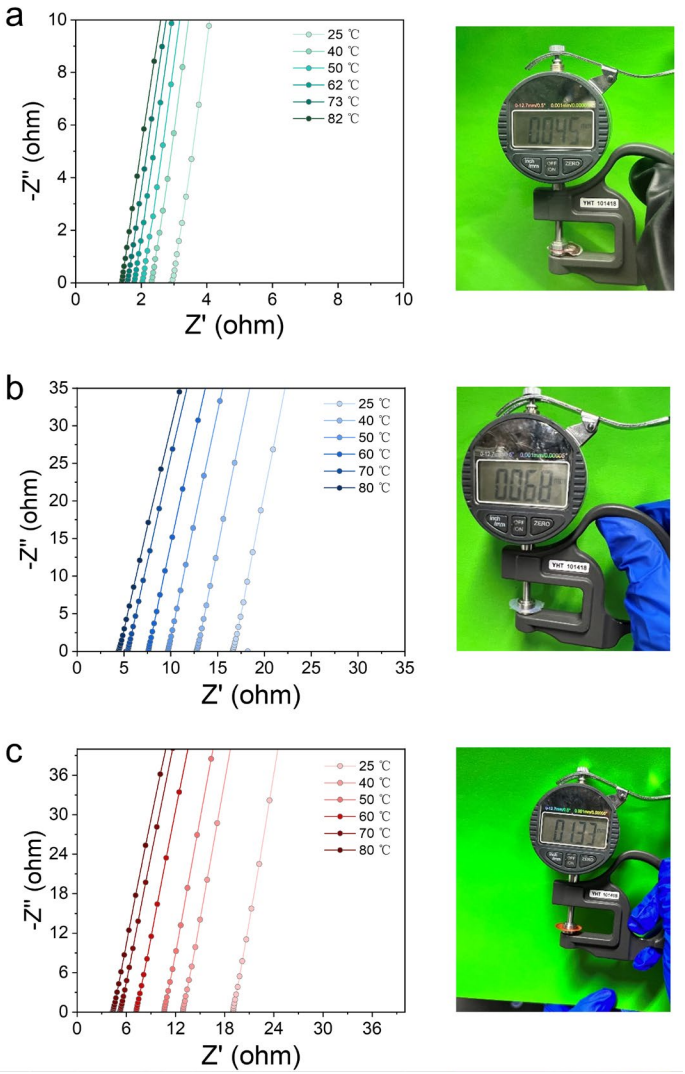

Figure S27. EIS Nyquist plots at different temperatures ranging from 10 °C to 60 °C and photographs of PACOF-8 (**a**), PANF (**b**) and PVHP-COF (**c**) electrolytes.

Note: To ensure that the surface resistance values exceed 0.5 Ω cm^{-2}, thereby eliminating the influence of contact impedance, we layered ten sheets of the host membranes to fabricate the final solid-state electrolyte membranes. Then EIS measurements of SS|SPE|SS were carried out from 25 to 80 ℃ to study Li^+ conduction properties.

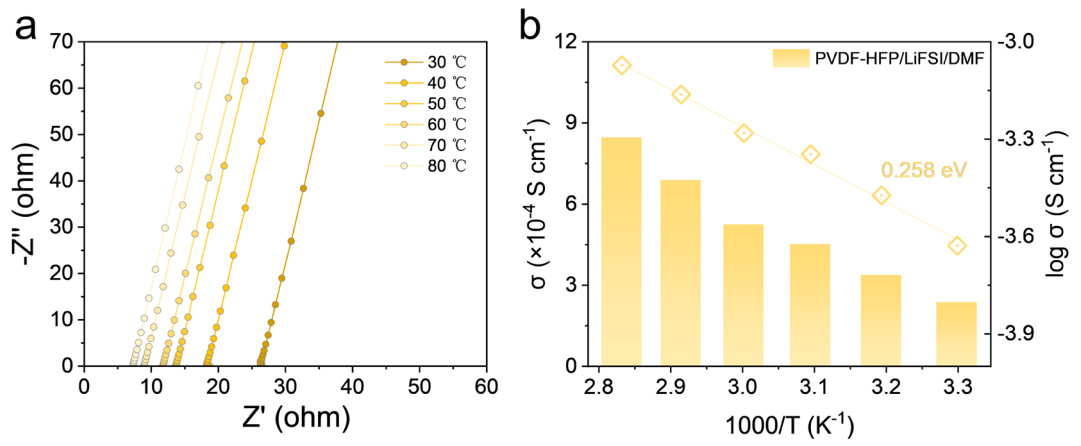

Figure S28. a, EIS Nyquist plots at different temperatures ranging from 10 °C to 60 °C of PVDF-HFP/LiFSI/DMF electrolyte. **b**, Arrhenius plots and calculated activation energy.

Note: By evaluating the ionic conductivity of the pure PVDF-HFP/LiFSI/DMF electrolyte across a range of temperatures from 25 to 80 ℃, it was proved that ANFs had no impact on the transport of lithium ions, exhibiting the same activation energy as the PANF electrolyte.

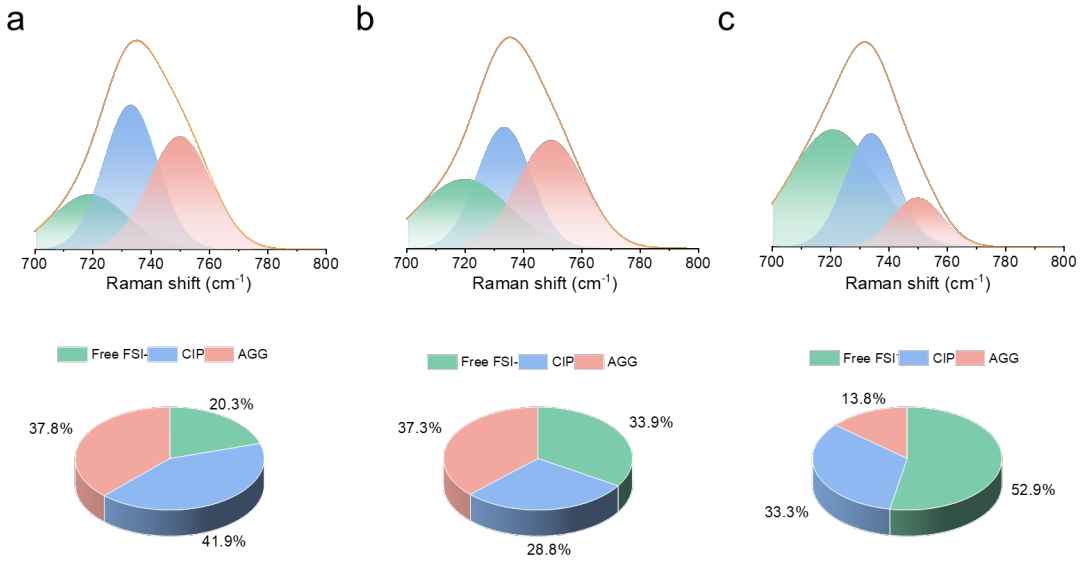

Figure S29. Raman spectra of the PANF (**a**), PVHP-COF (**b**) and PACOF-8 (**c**) electrolytes, along with corresponding quantification results for FSI^- states. CIP, contact ion pairs; AGGs, aggregate clusters.

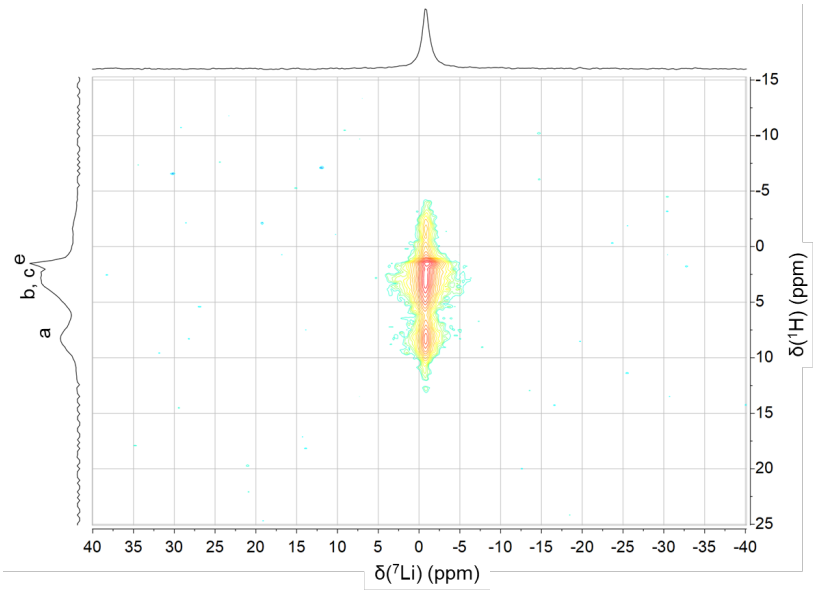

Figure S30. 2D ^{1}H–^{7}Li heteronuclear correlation (HETCOR) spectrum of COFs/DMF/LiFSI system measured with a CP contact time of 1 ms.

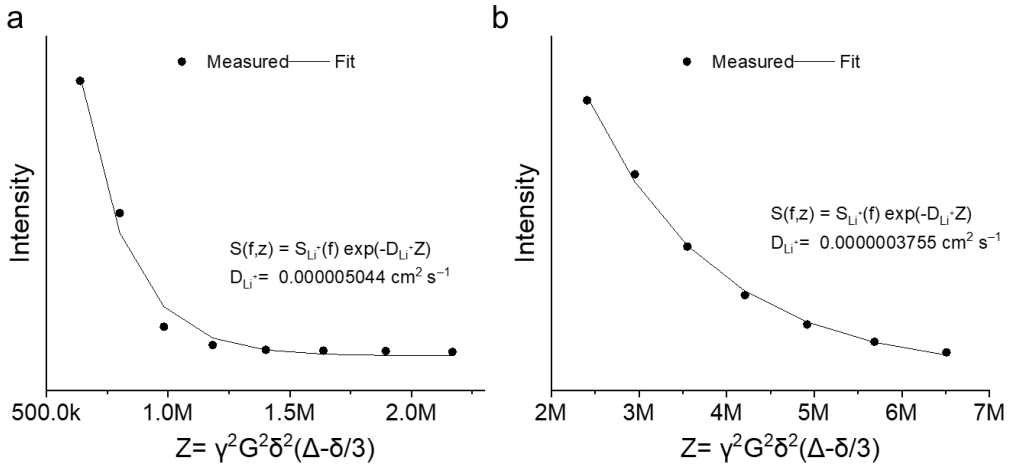

Figure S31. Li^{+} diffusion coefficient of NUS-9 and PVHP/LiFSI/DMF system tested by PEG-NMR.

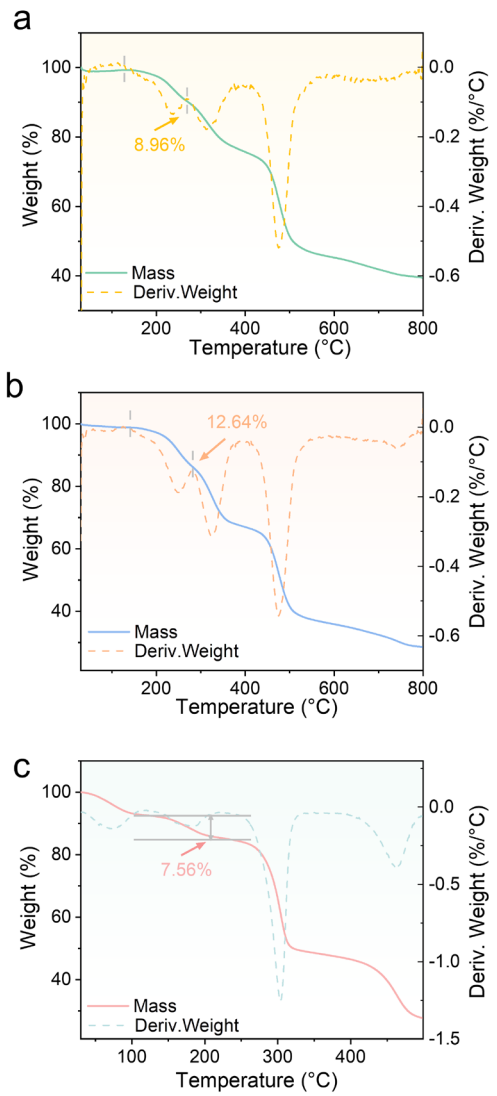

Figure S32. DMF solvent content tested by TGA. TG and DTA curves of PACOF-8 (**a**), PANF (**b**), PVHP-COF (**c**) electrolytes.

Note: The weight loss during 120 to 250 ℃ was attributed to the escape of DMF solvent molecules confined in electrolytes. As observed from the DTA curve, this process corresponded with the second peaks.

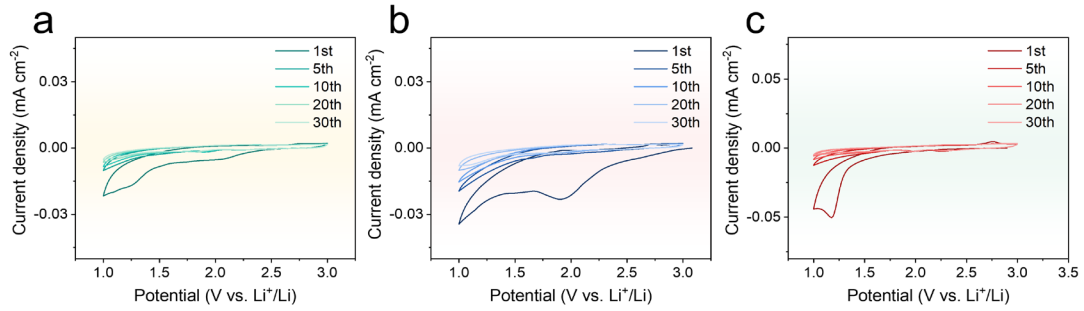

Figure S33. Cycle voltammetry curve of Li|SPE|Cu half cells using PACOF-8 (**a**), PANF (**b**) and PVHP-COF (**c**) electrolytes.

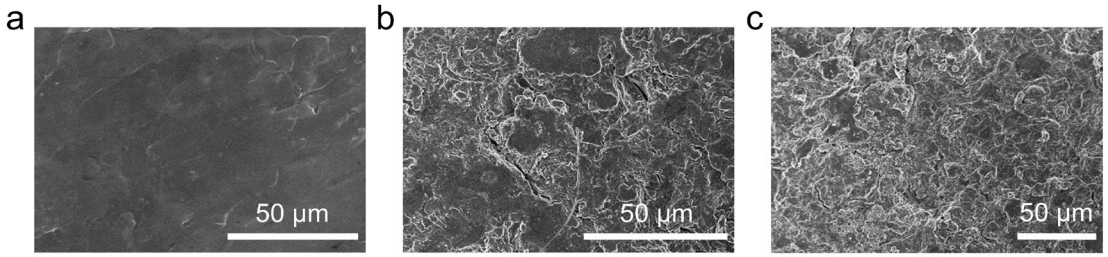

Figure S34. SEM images of Li anodes using PACOF-8 (**a**), PANF (**b**) and PVHP-COF (**c**) after cycling 200h.

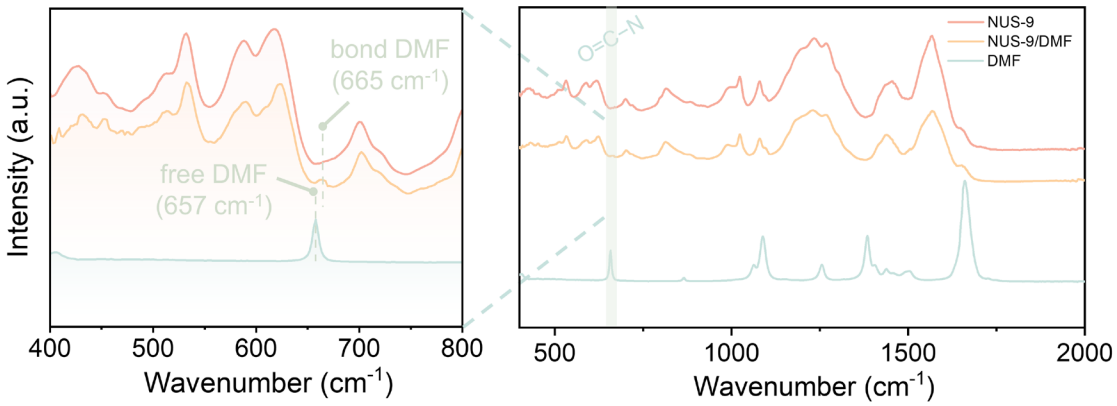

Figure S35. The capture effect of DMF solvent by COFs. FTIR spectra in the range of 400-800 cm^{-1} observed for pure DMF solvent, NUS-9 nanosheets and NUS-9/DMF composite.

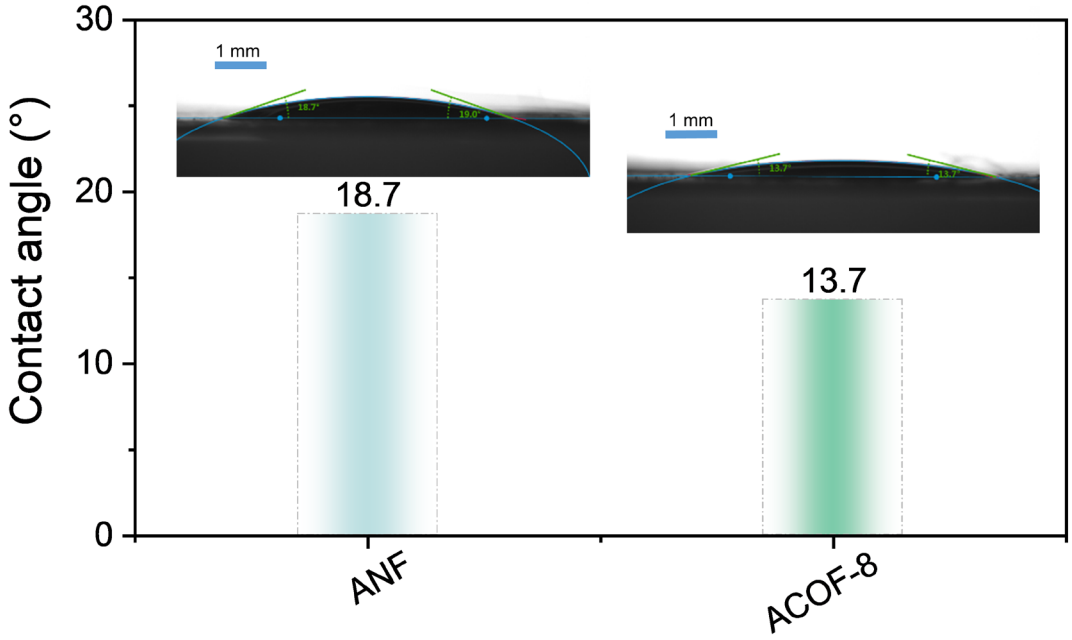

Figure S36. Contact angle mearurements of DMF against ANF and ACOF-8 membranes.

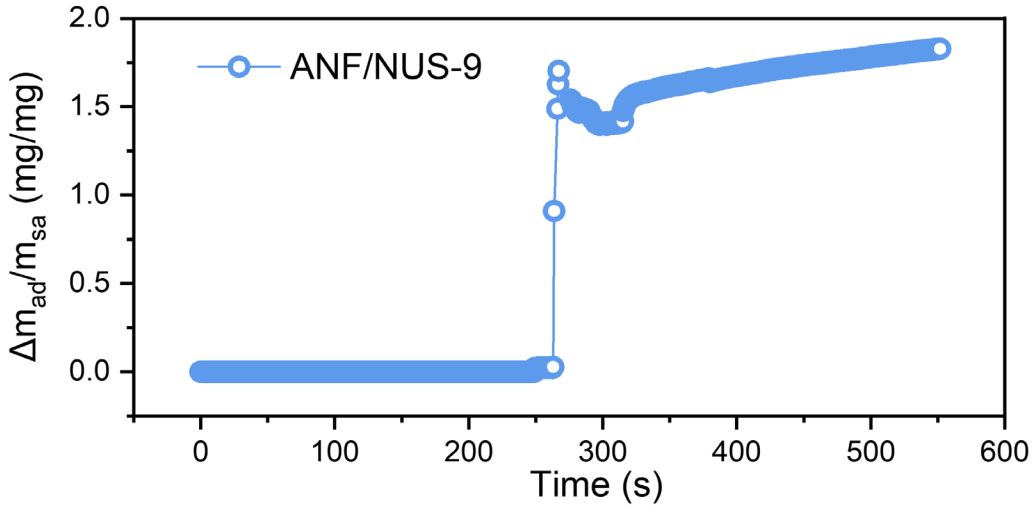

Figure S37. QCM spectra of ANF/NUS-9 mixture.

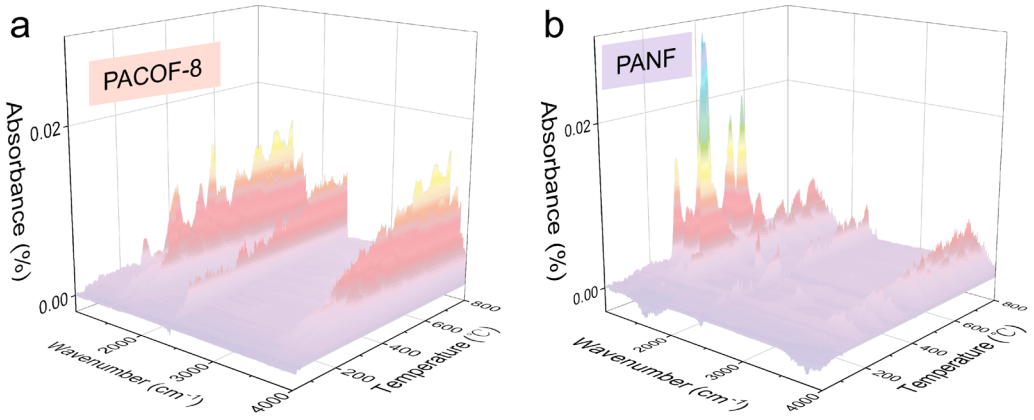

Figure S38. TG-FTIR of PACOF-8 (**a**) and PANF (**b**) electrolytes.

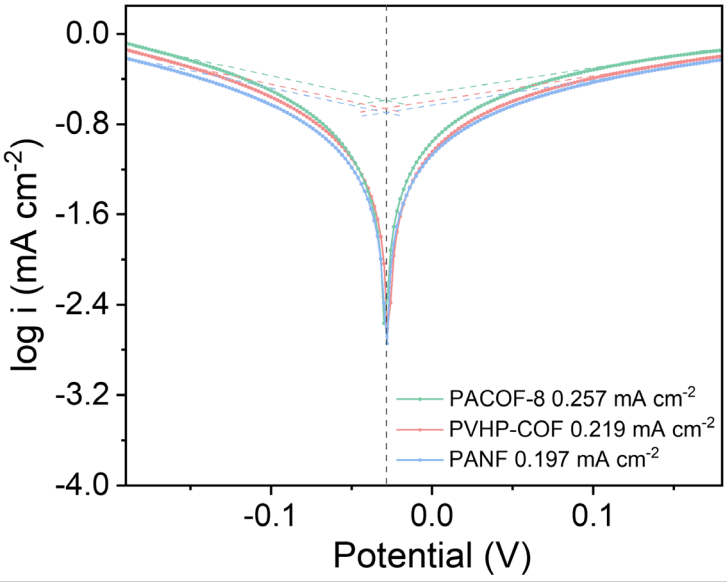

Figure S39. Tafel plots and estimated exchange current density of Li|Li symmetric cell paired with PACOF-8, PVHP-COF, PANF.

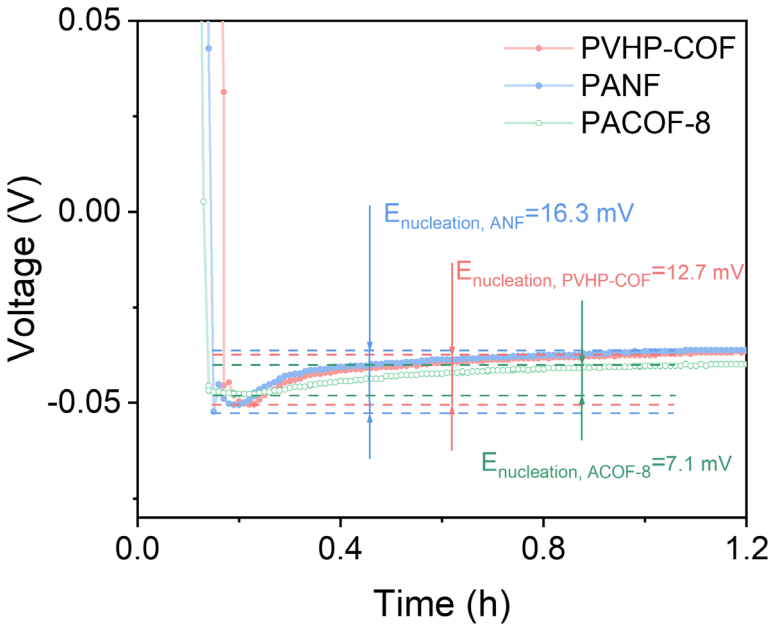

Figure S40. Voltage profiles of Li|Cu half cells using PVHP-COF, PANF, PACOF-8 under a constant current density of 0.1 mA cm^{-2}.

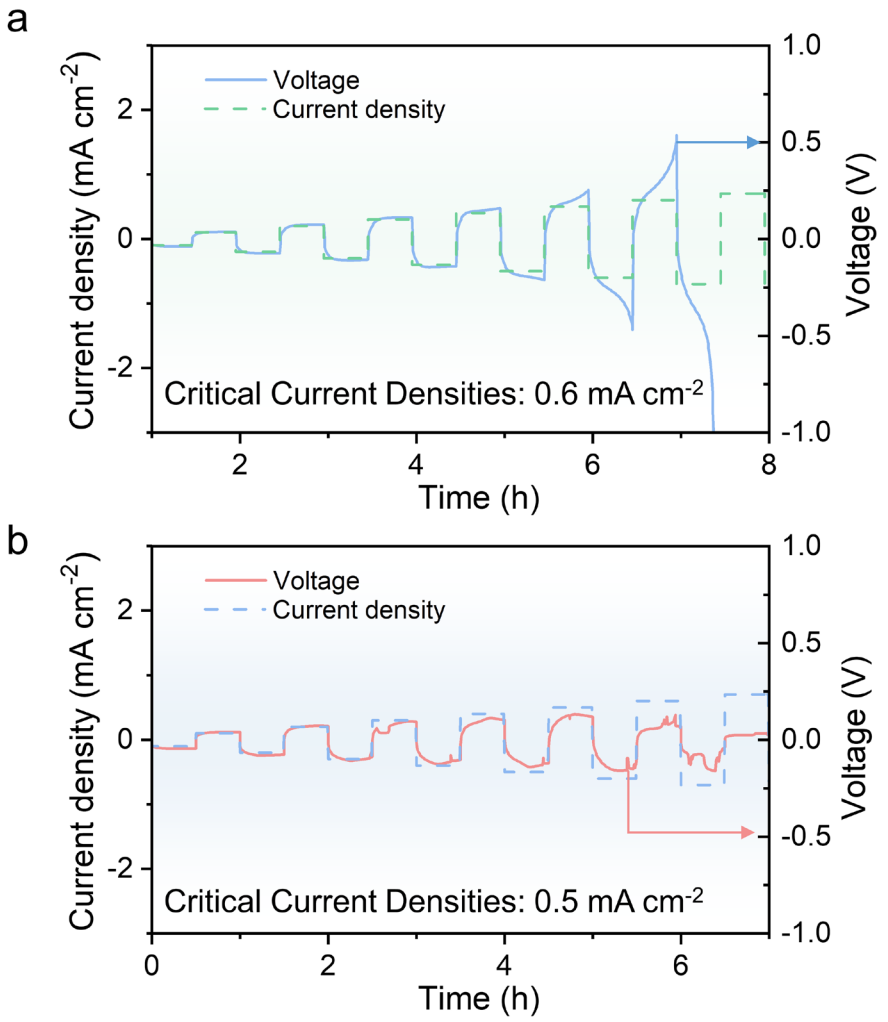

Figure S41. CCD test of PANF (**a**) and PVHP-COF (**b**) electrolytes.

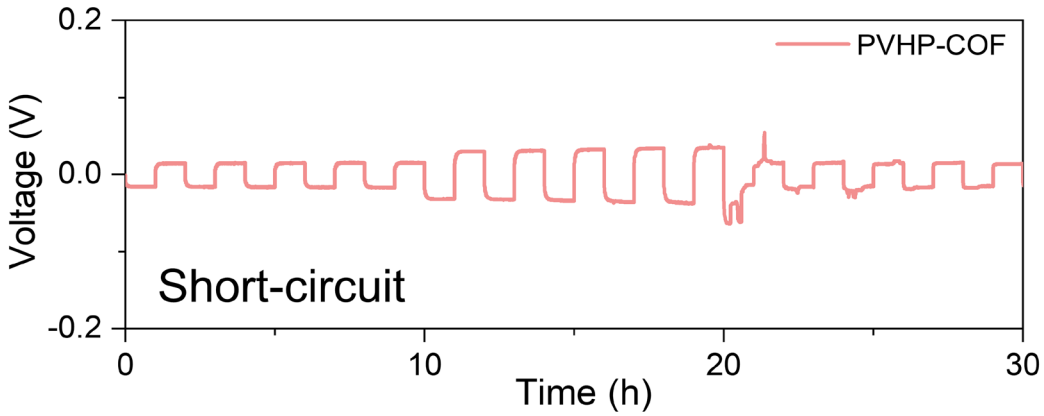

Figure S42. Galvanostatic cycling curves of Li||Li cells with PVHP-COF electrolyte at 0.2 mA cm^{-2} and 0.2 mAh cm^{-2}.

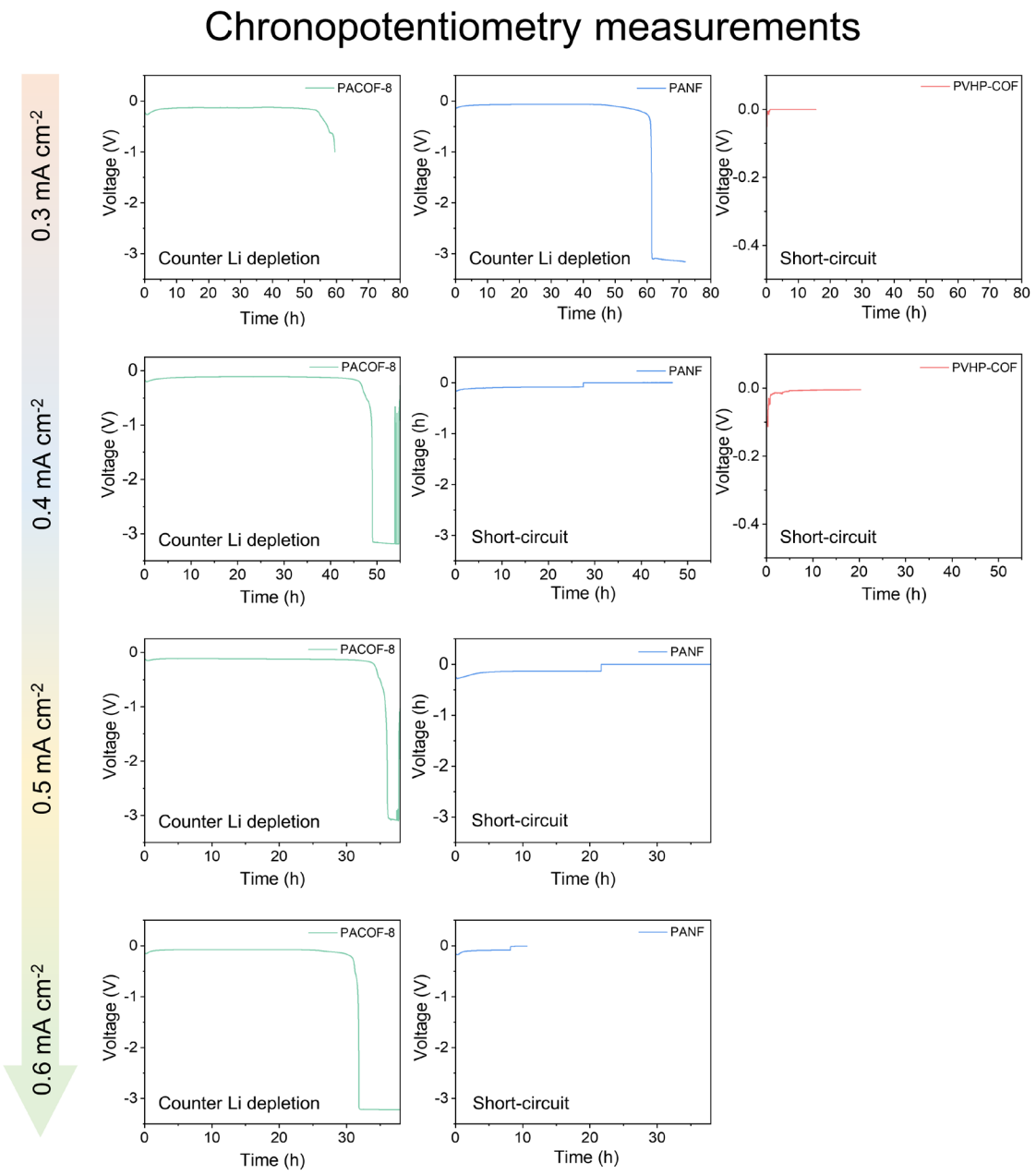

Figure S43. Chronopotentiometry measurements of Li-Li symmetric cells with PACOF-8, PANF, PVHP-COF electrolytes at different current density of 0.3-0.6 mA cm^{-2}.

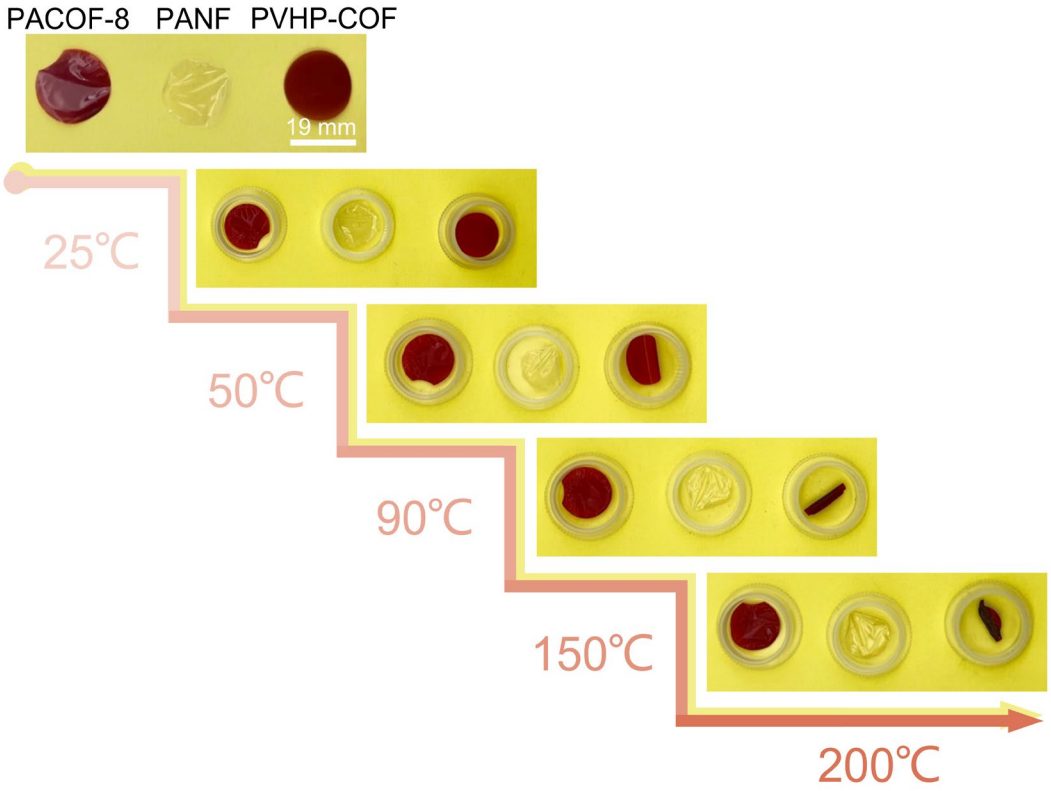

Figure S44. Optical photographs of PACOF-8, PANF, PVHP-COF heated to different temperatures ranging from RT to 200 ℃.

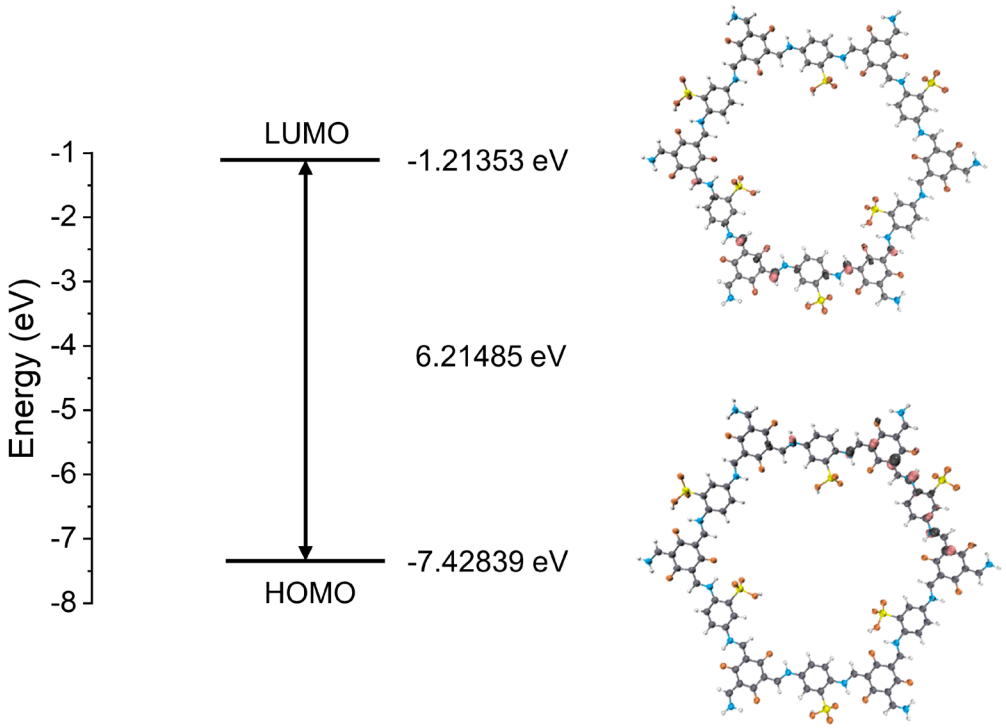

Figure S45. DFT analysis of HOMO and LUMO values for NUS-9 unit calculated by Gaussian 09.

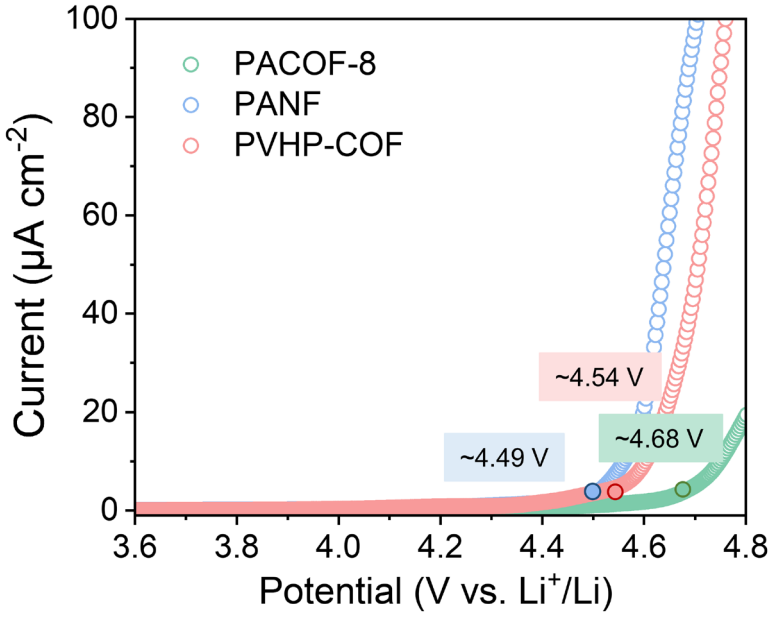

Figure S46. Linear sweep voltammetry (LSV) test results for PACOF-8, PANF and PVHP-COF electrolytes.

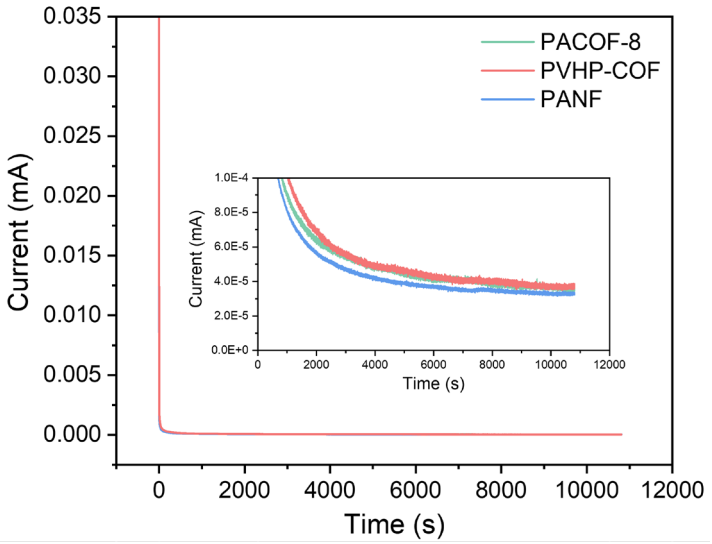

Electrolyte	Electronic conductivity (S cm^{-1})
PACOF-8	6.45×10^{-10}
PVHP-COF	7.00×10^{-10}
PANF	5.71×10^{-10}

Figure S47. Electronic conductivities tests for PACOF-8, PANF and PVHP-COF electrolytes.

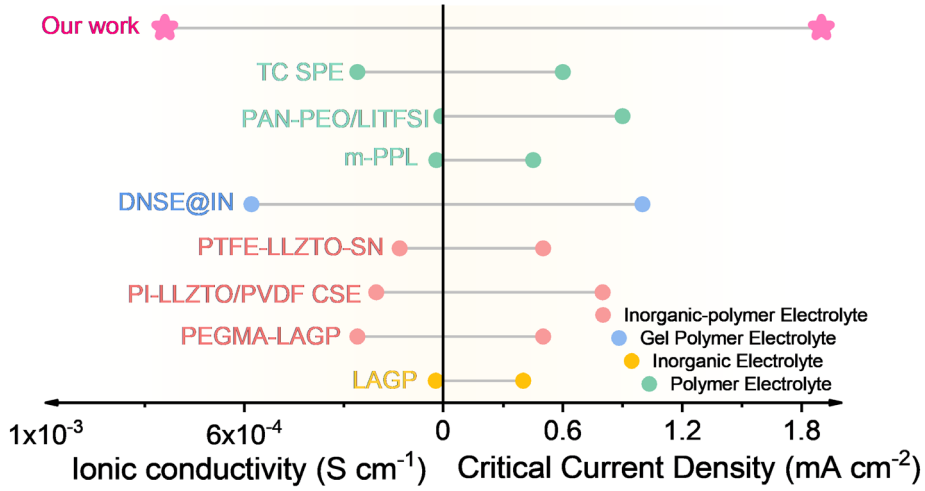

Figure S48. Comparison of ionic conductivity and critical current density of different types of electrolytes.

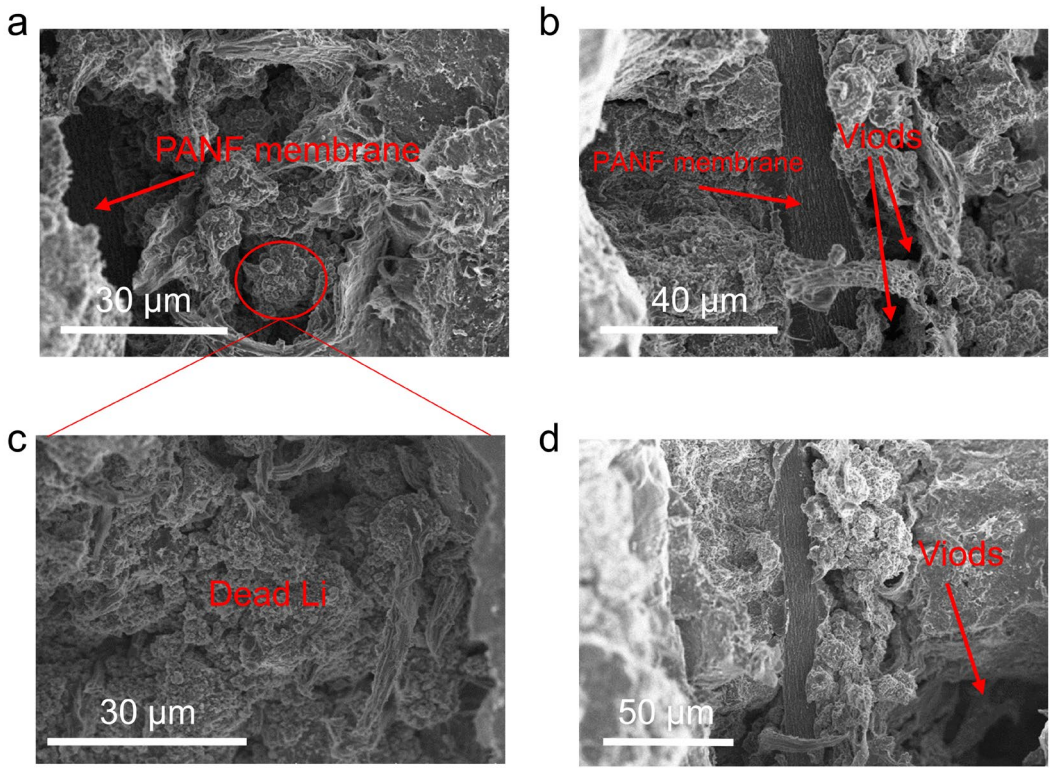

Figure S49. Cross-sectional SEM images of Li|PANF|Li symmetric cell with the contact loss failure.

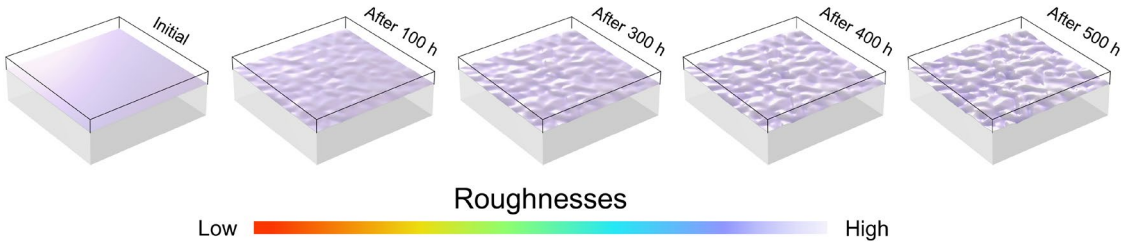

Figure S50. Alterations in the surface topography of the lithium anode using PACOF-8 electrolyte during cycling.

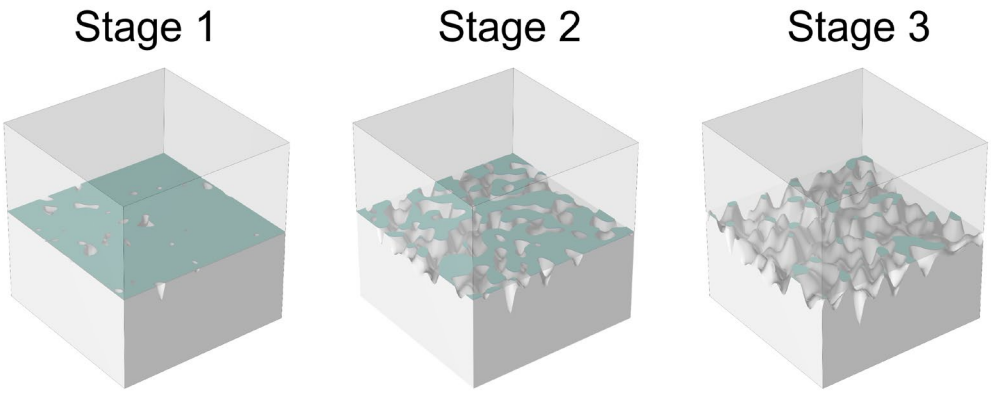

Figure S51. The physical model used for the finite-element simulations of cycling curves of Li|PANF|Li symmetrical cell at a current density of 0.8 mA cm^{-2}.

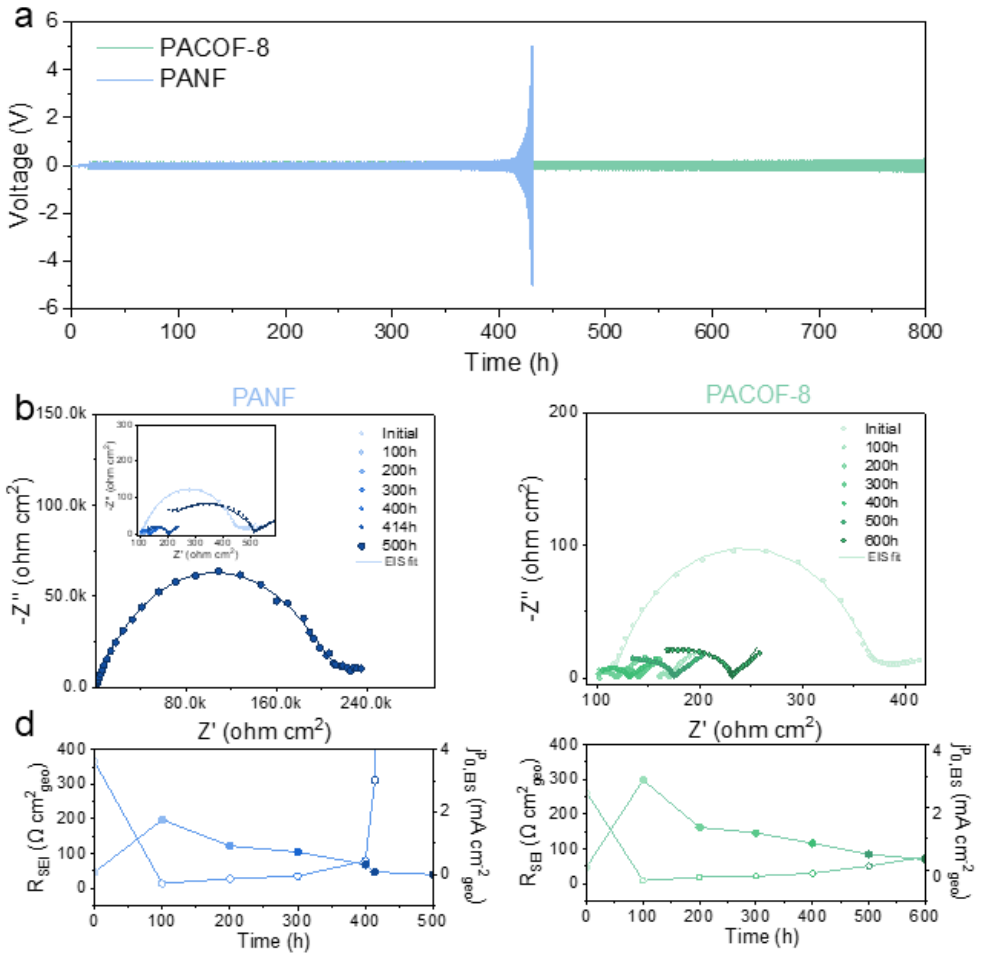

Figure S52. a, Galvanostatic cycling curves of Li||Li cells with PACOF-8, PANF electrolyte at 0.8 mA cm^{-2} and 0.2 mAh cm^{-2}. Nyquist plots of Li|PANF|Li cell (**b**) and

Li|PACOF-8|Li cell (**c**) after various hours of cycling. **d**, SEI resistance and pseudo-exchange current density, $j^{p}_{0,EIS}$ were obtained from fitting EIS spectra in (**b**).

Note: The equivalent circuit used to fit all EIS spectra in this study was based on models established in previous research[22]. An exchange current value was derived from the EIS fitting using the equation $j^{p}_{0,EIS} = kT/(eR_{\mathrm{SEI}})$, where k represents the Boltzmann constant, T denotes the temperature (set at 297 K), e is the elementary charge, and R_{SEI} is the total resistance of SEI. In most of the electrolytes examined, the EIS spectrum measured before cycling exhibited the highest magnitude. This phenomenon is largely due to the formation of an extraneous surface film during cell assembly[23]. In subsequent cycles, fresh lithium surfaces become exposed, leading to a reduction of R_{SEI}. Regrettably, the R_{SEI} of the Li|PANF system increased over the course of cycling because of severe side reactions occurring at the interface, in parallel with rapid downturn of $j^{p}_{0,EIS}$.

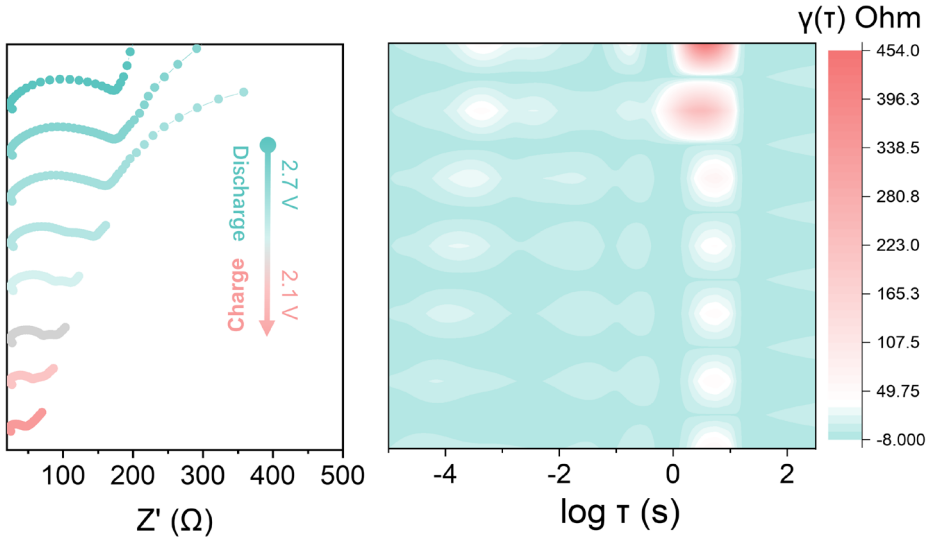

Figure S53. Nyquist plots collected from in situ EIS test of PVHP-COF and corresponding contour plots from the calculated DRT results.

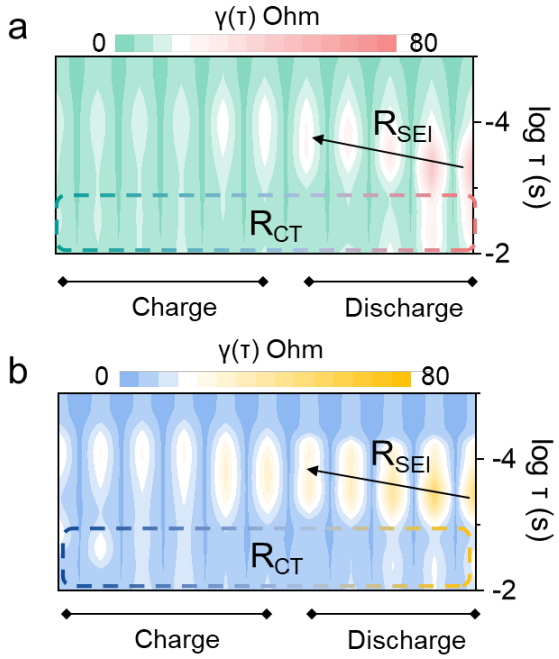

Figure S54. DRT transition results of Li|PANF|SPAN (**a**) and Li|PACOF-8|SPAN (**b**) full cells

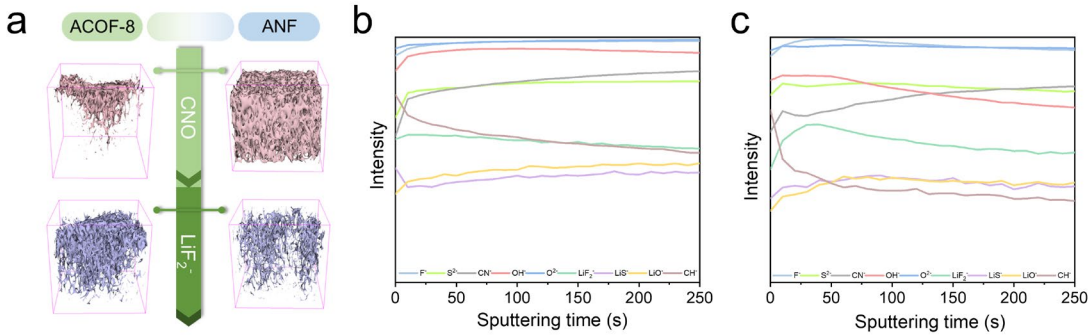

Figure S55. a TOF-SIMS 3D view in the formed SEI with different electrolytes after 20 cycles. TOF-SIMS depth profiles of the secondary ion fragments in the formed SEI by PANF (**b**) and PACOF-8 (**c**) electrolytes.

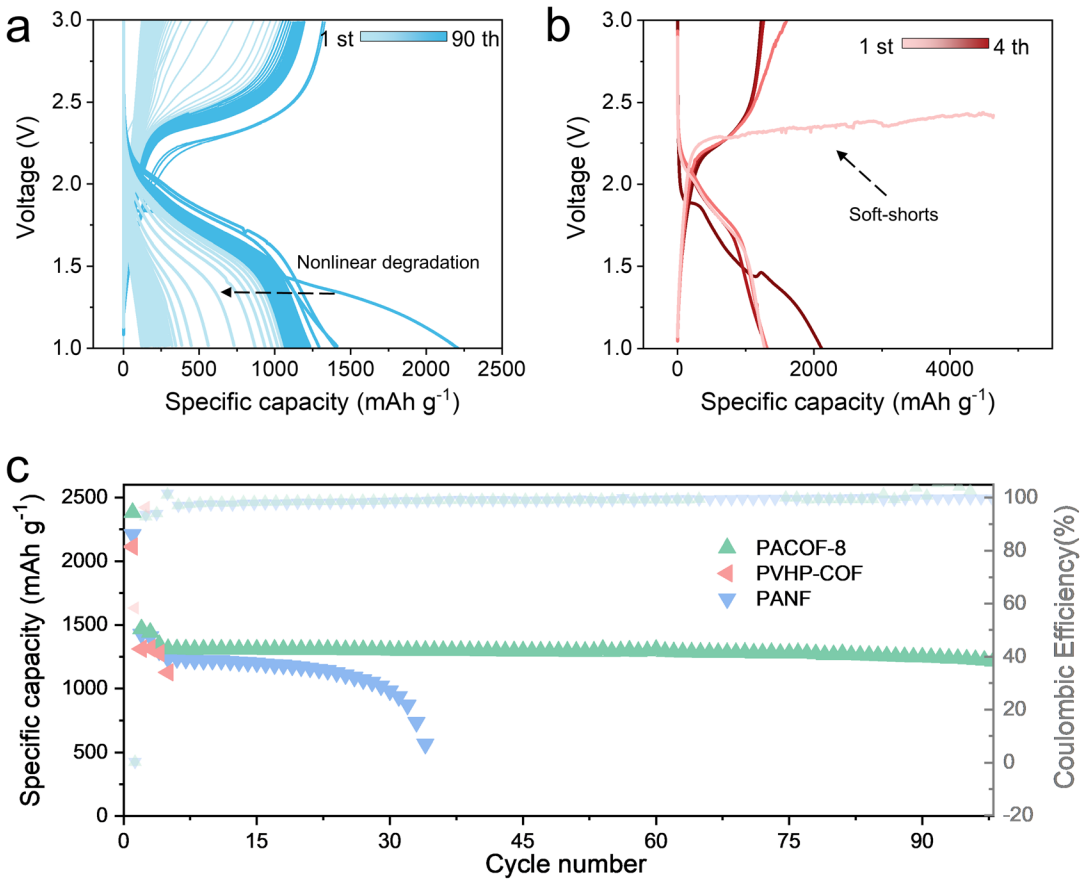

Figure S56. The charge/discharge voltage profiles of Li|PANF|SPAN (**a**) and Li|PVHP-COF|SPAN (**b**) full cell. **c** Cycling stability of the SPAN|Li solid-state batteries with an active material SPAN loading of 2.0 mg.

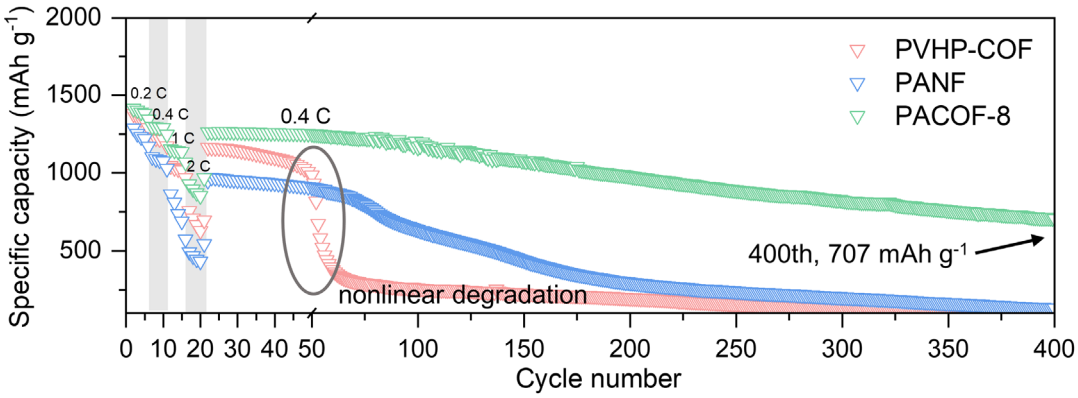

Figure S57. Rate and cycling performance of the Li||SPAN batteries.

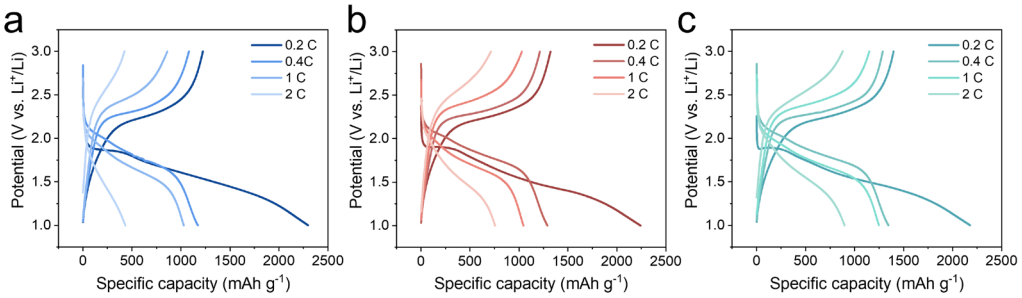

Figure S58. Comparison of the charge/discharge profiles of SPAN|PANF| Li (a), SPAN|PVHP-COF|Li (b) and SPAN|PACOF-8|Li full cells at different rates.

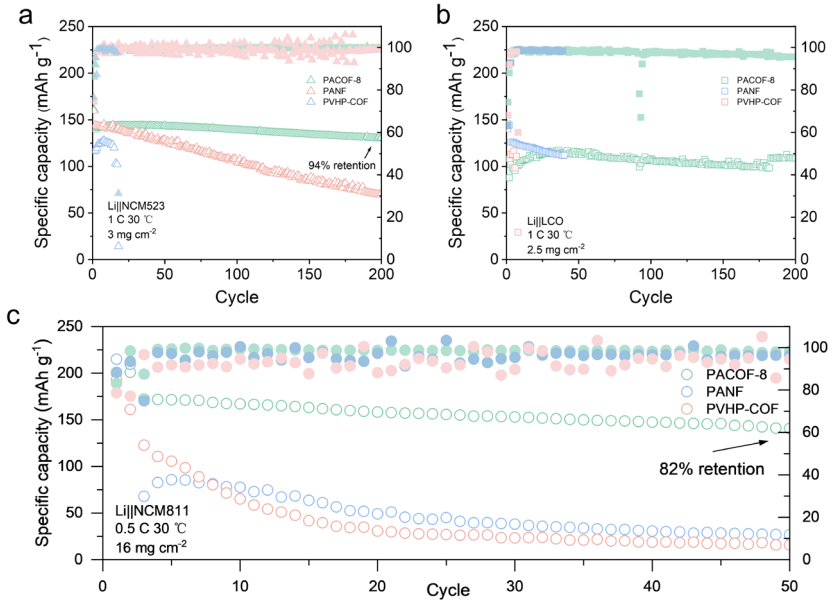

Figure S59. Cycling stability of Li|NCM523 (**a**), Li|LCO (**b**) and Li|NCM811 (**c**) solid-state batteries using PANF, PACOF-8 and PVHP-COF electrolytes

Note: To further evaluate the electrolyte designs, electrochemical performances of Li|NCM523 and Li|NCM811 were tested with a charge cut-off voltage of 4.3 V using three SPEs. Two formation cycles at 0.1 C were conducted for SEI formation before long-term cycling for both charge and discharge of the cells. As shown in Fig. S a, the cell with PACOF-8 electrolyte shows the best long-term cycling performance, with 94% capacity retention after 200 cycles (specific capacity of 139.44/ 130.59 mAh g^{-1} for 3th/200th cycle). In contrast, the cell with PANF electrolyte exhibits poor long-term cycling performance, with only 49% capacity retention after 200 cycles (specific capacity of 143.45/ 71.33 mAh g^{-1} for 3th/200th cycle). Even with a NCM811 loading of 16 mg cm^{-2}, the capacity retention of Li|PACOF-8|NCM811 reaches 82% after 50 cycles, while that using PANF and PVHP-COF presents rapid capacity loss over several cycles (Fig. S c). Moreover, Li|LCO were tested with a charge cut-off voltage of 4.2 V using different SPEs in Fig. S b. The cell with the PACOF-8 electrolyte undergoes an activation process characterized by capacity growth, whereas the Li|PANF|LCO cell exhibits degradation over time. The Li|PVHP-COF|LCO cell displayed short circuit after 5 cycles.

Table S1 Comparison of mechanical strength and fabrication methods for representative COF membranes.

Materials	Preparation method	Thickness (μm)	Tensile strength (MPa)	Ref.
SPC-COF-NS	solution-casting	25	24.3	[24]
COF-QA-DOH(P)	solution-casting	\	49	[25]
IPC-COF	filtration	\	91.2	[26]
DLC	thermal pressing	32	22	[27]
TpPa-1	filtration	\	20.8	[28]
TpBD	filtration	\	21.2	[28]
TpHZ	filtration	\	14.6	[28]
$TpBD(OH)_2$	filtration	\	25.3	[28]
CNF@COF	filtration	\	40.2	[29]
COF-42	interfacial polymerization	87	0.27	[30]
PTSA@TpAzoCOFM	solution-casting	100-300	17	[31]
$TaPa\text{-}SO_3H$	solution-casting	20.7	40	[32]
DaTp	solution-casting	25-100	12	[33]
ANF	self-assembly	5	544.68	This work
ACOF-2	self-assembly	5	339.61	This work
ACOF-4	self-assembly	5	450.18	This work
ACOF-8	self-assembly	5	525.36	This work

Table S2 Comparison of symmetrical cells for the reported SSEs consisted of electrolytes based on PVDF or PVDF-HFP.

Materials	Temperature (°C)	Current density (mA cm^{-2})	Areal capacity (mAh cm^{-2})	Cumulative plated capacity (mAh cm^{-2})	Time (h)	Ref.
PVDF-GCN	RT	0.1	0.1	220	2200	[34]
GPE-0.8	30	0.1	0.1	100	1000	[35]
CPE with LiF	20	0.2	0.1	80	800	[36]
PI-LLZTO/ PVDF CSE	25	0.1	0.1	100	1000	[37]
P(VDF-TrFE-CTFE)	25	0.05	0.05	60	1200	[38]
PVHLi-1.1	40	0.3	0.15	60	400	[39]
$F{-}Mo_2C{-}LCPP$	RT	0.1	0.05	10	200	[40]
PMLSE	25	0.25	0.125	212.5	1700	[41]
PLLDB	RT	0.25	0.125	33.75	270	[42]
CPE-2	RT	0.1	0.1	100	1000	[43]
FPH-Li	30	0.1	0.1	90	900	[44]
PTC iono-SPE	25	0.1	0.05	75	1500	[45]
PVT-10CuPcLi	RT	0.2	0.2	400	2000	[46]
PVDF–LiFSI	25	0.1	0.1	200	2000	[47]
es-PVDF-PEO-GDC	50	0.4	0.2	130	650	[48]
LNFP50	25	0.5	0.5	450	900	[49]
PNNO-5	RT	0.1	0.1	280	2800	[50]
PACOF-8	30	0.2	0.2	500	2500	This work

Table S3 Comparison of thickness and thermal stability for the reported SSEs.

Materials	Class	Thickness (μm)	Thermal stability (℃)	Ref.
PAN-PEO/LiTFSI	SPE	5	150	[51]
FMC-ASPE-Li	SPE	200	120	[52]
Li|90% (BPSO-150% LiTFSI)-10% PVDF+CA	SPE	120	130	[53]
Zr-F4	IPCs	91	150	[54]
PVDF-LPPO SPEs	SPE	75	200	[55]
LTO-8	IPCs	33.67	180	[56]
EACN	IPCs	73	150	[57]
PACOF-8	SPE	5.6	200	This work

Note: inorganic–polymer composites (IPCs)

Table S4 Comparison of full cells performance (based on S/SPAN cathodes) for the reported SSEs.

Materials	Temperature (℃)	Cathodes	Rate/Specific capacity (mAh g^{-1})	Cycles/Average capacity decay (%)	Liquid additive	Ref.
GPE	RT	S/C	2 C/250	300/0.103	50% LE	[58]
GPE-0.8	70	S/C	0.5 C/400	NA	NA	[59]
PEO–Li–Zr	37	S/C	NA	80/0.5	IL	[60]
LiTFSI in PVDF-HFP/PMMA/SiO2	25	S/GNS	1 C/316	50/0.98	71% LE	[61]
AHE	25	S@CMK/3	1 C/792	NA	LE	[62]
PETEA-based GPE	25	S/C	1 C/601.2	100/0.366	LE	[63]
90% (BPSO-150% LiTFSI)-10% PVDF+CA	25	MCNT@S	1 C/495.3	80/0.12	DMF	[53]
LPS	50	S/C	1 C/237.3	100/0.15	NA	[64]
LLZO	60	SPAN/LiFSI/NGW	0.5 C/407	NA	NA	[65]
Poly(DOL)/PEG–SiO2 Hybrid SPE	RT	SPAN	1 C/200	100/0.56	NA	[66]
CGPE	RT	SPAN	1.5 C/489	180/0.052	LE	[67]
1PVHF1FSI	25	SPAN	1 C/923	100/0.323	13% DMF	[68]
GPE(Na|SPAN)	25	SPAN	1 C/962	63/0.49	LE	[69]
IDCN	25	S/C	0.2 C/1110	200/0.177	8.5% DOL	[70]
PACOF-8	30	SPAN	2 C/896	1000/0.0493	8.96% DMF	This work

References

1. M. Wang, P. Zhang, X. Liang, J. Zhao, Y. Liu, Y. Cao, H. Wang, Y. Chen, Z. Zhang, F. Pan, Z. Zhang and Z. Jiang, *Nature Sustainability*, 2022, **5**, 518-526.
2. B. Yang, L. Wang, M. Zhang, J. Luo and X. Ding, *ACS Nano*, 2019, **13**, 7886-7897.
3. M. J. Frisch, G. Trucks, H. B. Schlegel, G. E. Scuseria, M. A. Robb, J. Cheeseman, G. Scalmani, V. Barone, B. Mennucci, G. A. Petersson, H. Nakatsuji, M. Caricato, X. Li, H. P. Hratchian, A. F. Izmaylov, J. Bloino, G. Zheng, J. Sonnenberg, M. Hada and D. Fox, 2009.
4. S. Plimpton, *Journal of Computational Physics*, 1995, **117**, 1-19.
5. T. D. Kühne, M. Iannuzzi, M. Del Ben, V. V. Rybkin, P. Seewald, F. Stein, T. Laino, R. Z. Khaliullin, O. Schütt, F. Schiffmann, D. Golze, J. Wilhelm, S. Chulkov, M. H. Bani-Hashemian, V. Weber, U. Borštnik, M. Taillefumier, A. S. Jakobovits, A. Lazzaro, H. Pabst, T. Müller, R. Schade, M. Guidon, S. Andermatt, N. Holmberg, G. K. Schenter, A. Hehn, A. Bussy, F. Belleflamme, G. Tabacchi, A. Glöß, M. Lass, I. Bethune, C. J. Mundy, C. Plessl, M. Watkins, J. VandeVondele, M. Krack and J. Hutter, *J Chem Phys*, 2020, **152**, 194103.
6. J. VandeVondele, M. Krack, F. Mohamed, M. Parrinello, T. Chassaing and J. Hutter, *Computer Physics Communications*, 2005, **167**, 103-128.
7. N. Mardirossian and M. Head-Gordon, *J Chem Phys*, 2016, **144**, 214110.
8. N. Mardirossian and M. Head-Gordon, *J Chem Phys*, 2016, **144**, 214110.
9. T. Lu and Q. Chen, *Chemistry Methods*, 2021, **1**, 231-239.
10. T. Lu and F. Chen, *Journal of Computational Chemistry*, 2012, **33**, 580-592.
11. W. Humphrey, A. Dalke and K. Schulten, *Journal of Molecular Graphics*, 1996, **14**, 33-38.
12. T. Lu and Q. Chen, *Theoretical Chemistry Accounts*, 2020, **139**.
13. U. Salzner and A. Aydin, *Journal of Chemical Theory and Computation*, 2011, **7**, 2568-2583.
14. T. Lu and Q. Chen, *Journal of Computational Chemistry*, 2022, **43**, 539-555.
15. F. Neese, *WIREs Computational Molecular Science*, 2022, **12**, e1606.
16. S. Grimme, A. Hansen, S. Ehlert and J.-M. Mewes, *J Chem Phys*, 2021, **154**, 064103.
17. M. Doyle, J. Newman, A. S. Gozdz, C. N. Schmutz and J. M. Tarascon, *Journal of The Electrochemical Society*, 1996, **143**, 1890.
18. T. Lu and Q. Chen, *Chemistry–Methods*, 2021, **1**, 231-239.
19. S. R. Kwon, M. B. Elinski, J. D. Batteas and J. L. Lutkenhaus, *ACS applied materials & interfaces*, 2017, **9**, 17125-17135.
20. Y. Ying, S. B. Peh, H. Yang, Z. Yang and D. Zhao, *Advanced Materials*, 2022, **34**, 2104946.
21. H. Wang, Y. Zhai, Y. Li, Y. Cao, B. Shi, R. Li, Z. Zhu, H. Jiang, Z. Guo, M. Wang, L. Chen, Y. Liu, K.-G. Zhou, F. Pan and Z. Jiang, *Nature Communications*, 2022, **13**, 7123.
22. G. M. Hobold, K.-H. Kim and B. M. Gallant, *Energy & Environmental Science*, 2023, **16**, 2247-2261.
23. D. Aurbach and A. Zaban, *Journal of Electroanalytical Chemistry*, 1994, **365**, 41-45.
24. T. Huang, H. Jiang, J. C. Douglin, Y. Chen, S. Yin, J. Zhang, X. Deng, H. Wu, Y. Yin, D. R. Dekel, M. D. Guiver and Z. Jiang, *Angewandte Chemie International Edition*, 2023, **62**, e202209306.
25. Z. Guo, H. Jiang, H. Wu, L. Zhang, S. Song, Y. Chen, C. Zheng, Y. Ren, R. Zhao, Y. Li, Y. Yin, M. D. Guiver and Z. Jiang, *Angewandte Chemie International Edition*, 2021, **60**, 27078-

27085.
26. L. Cao, H. Wu, Y. Cao, C. Fan, R. Zhao, X. He, P. Yang, B. Shi, X. You and Z. Jiang, *Advanced Materials*, 2020, **32**, 2005565.
27. D. Guo, D. B. Shinde, W. Shin, E. Abou-Hamad, A.-H. Emwas, Z. Lai and A. Manthiram, *Advanced Materials*, 2022, **34**, 2201410.
28. H. Yang, L. Yang, H. Wang, Z. Xu, Y. Zhao, Y. Luo, N. Nasir, Y. Song, H. Wu, F. Pan and Z. Jiang, *Nature Communications*, 2019, **10**, 2101.
29. X. Kong, Z. Wu, M. Strømme and C. Xu, *Journal of the American Chemical Society*, 2024, **146**, 742-751.
30. Z. Wang, Q. Yu, Y. Huang, H. An, Y. Zhao, Y. Feng, X. Li, X. Shi, J. Liang, F. Pan, P. Cheng, Y. Chen, S. Ma and Z. Zhang, *ACS Central Science*, 2019, **5**, 1352-1359.
31. H. S. Sasmal, H. B. Aiyappa, S. N. Bhange, S. Karak, A. Halder, S. Kurungot and R. Banerjee, *Angewandte Chemie International Edition*, 2018, **57**, 10894-10898.
32. S. Hou, W. Ji, J. Chen, Y. Teng, L. Wen and L. Jiang, *Angewandte Chemie International Edition*, 2021, **60**, 9925-9930.
33. A. Khayum M, V. Vijayakumar, S. Karak, S. Kandambeth, M. Bhadra, K. Suresh, N. Acharambath, S. Kurungot and R. Banerjee, *ACS Applied Materials & Interfaces*, 2018, **10**, 28139-28146.
34. L. Chen, T. Gu, J. Ma, K. Yang, P. Shi, J. Biao, J. Mi, M. Liu, W. Lv and Y.-B. He, *Nano Energy*, 2022, **100**, 107470.
35. L. Chen, L. Cheng, J. Yu, J. Chu, H.-g. Wang, F. Cui and G. Zhu, *Adv. Funct. Mater.*, 2022, **32**, 2209848.
36. S. Bag, C. Zhou, P. J. Kim, V. G. Pol and V. Thangadurai, *Energy Storage Materials*, 2020, **24**, 198-207.
37. J. Hu, P. He, B. Zhang, B. Wang and L.-Z. Fan, *Energy Storage Materials*, 2020, **26**, 283-289.
38. Y.-F. Huang, T. Gu, G. Rui, P. Shi, W. Fu, L. Chen, X. Liu, J. Zeng, B. Kang, Z. Yan, F. J. Stadler, L. Zhu, F. Kang and Y.-B. He, *Energy & Environmental Science*, 2021, **14**, 6021-6029.
39. W. Liu, C. Yi, L. Li, S. Liu, Q. Gui, D. Ba, Y. Li, D. Peng and J. Liu, *Angew. Chem. Int. Ed. Engl.*, 2021, **60**, 12931-12940.
40. Y. Shan, L. Li, X. Chen, S. Fan, H. Yang and Y. Jiang, *ACS Energy Letters*, 2022, **7**, 2289-2296.
41. J. Sun, X. Yao, Y. Li, Q. Zhang, C. Hou, Q. Shi and H. Wang, *Adv. Funct. Mater.*, 2020, **10**, 2000709.
42. M. Li, H. An, Y. Song, Q. Liu, J. Wang, H. Huo, S. Lou and J. Wang, *Journal of the American Chemical Society*, 2023, **145**, 25632-25642.
43. Y. Xu, K. Wang, X. Zhang, Y. Ma, Q. Peng, Y. Gong, S. Yi, H. Guo, X. Zhang, X. Sun, H. Gao, S. Xin, Y.-G. Guo and Y. Ma, *Advanced Energy Materials*, 2023, **13**, 2204377.
44. P. Zhai, Z. Yang, Y. Wei, X. Guo and Y. Gong, *Advanced Energy Materials*, 2022, **12**, 2200967.
45. J.-F. Liu, Z.-Y. Wu, F. J. Stadler and Y.-F. Huang, 2023, **62**, e202300243.
46. H. Wang, H. Cheng, D. Li, F. Li, Y. Wei, K. Huang, B. Jiang, H. Xu and Y. Huang, 2023, **13**, 2204425.
47. X. Zhang, S. Wang, C. Xue, C. Xin, Y. Lin, Y. Shen, L. Li and C.-W. Nan, 2019, **31**, 1806082.

48. L. Gao, S. Luo, J. Li, B. Cheng, W. Kang and N. Deng, *Energy Storage Materials*, 2021, **43**, 266-274.
49. B. Peng, Z. Liu, Q. Zhou, X. Xiong, S. Xia, X. Yuan, F. Wang, K. I. Ozoemena, L. Liu, L. Fu and Y. Wu, **n/a**, 2307142.
50. J. Zhu, S. He, H. Tian, Y. Hu, C. Xin, X. Xie, L. Zhang, J. Gao, S.-M. Hao, W. Zhou and L. Zhang, *Adv. Funct. Mater.*, 2023, **33**, 2301165.
51. D. Zhang, M. Liu, J. Ma, K. Yang, Z. Chen, K. Li, C. Zhang, Y. Wei, M. Zhou, P. Wang, Y. He, W. Lv, Q.-H. Yang, F. Kang and Y.-B. He, *Nature Communications*, 2022, **13**, 6966.
52. Y. Su, X. Rong, A. Gao, Y. Liu, J. Li, M. Mao, X. Qi, G. Chai, Q. Zhang, L. Suo, L. Gu, H. Li, X. Huang, L. Chen, B. Liu and Y.-S. Hu, *Nature Communications*, 2022, **13**, 4181.
53. L. Chen and L. Z. Fan, *Energy Storage Materials*, 2018, **15**, 37-45.
54. W. Huang, S. Wang, X. Zhang, Y. Kang, H. Zhang, N. Deng, Y. Liang and H. Pang, *Advanced Materials*, 2023, **35**, 2310147.
55. J. Mi, J. Ma, L. Chen, C. Lai, K. Yang, J. Biao, H. Xia, X. Song, W. Lv, G. Zhong and Y.-B. He, *Energy Storage Materials*, 2022, **48**, 375-383.
56. Q. Zhou, X. Yang, X. Xiong, Q. Zhang, B. Peng, Y. Chen, Z. Wang, L. Fu and Y. Wu, *Advanced Energy Materials*, 2022, **12**, 2201991.
57. Y. Zhao, J. Yan, W. Cai, Y. Lai, J. Song, J. Yu and B. Ding, *Energy Storage Materials*, 2019, **23**, 306-313.
58. Y. Xia, Y. F. Liang, D. Xie, X. L. Wang, S. Z. Zhang, X. H. Xia, C. D. Gu and J. P. Tu, *Chemical Engineering Journal*, 2019, **358**, 1047-1053.
59. A. Unemoto, H. Ogawa, Y. Gambe and I. Honma, *Electrochimica Acta*, 2014, **125**, 386-394.
60. O. Sheng, C. Jin, J. Luo, H. Yuan, C. Fang, H. Huang, Y. Gan, J. Zhang, Y. Xia, C. Liang, W. Zhang and X. Tao, *Journal of Materials Chemistry A*, 2017, **5**, 12934-12942.
61. Y. Zhang, Y. Zhao and Z. Bakenov, *Nanoscale Research Letters*, 2014, **9**, 137.
62. M. Liu, H. R. Jiang, Y. X. Ren, D. Zhou, F. Y. Kang and T. S. Zhao, *Electrochimica Acta*, 2016, **213**, 871-878.
63. M. Liu, D. Zhou, Y.-B. He, Y. Fu, X. Qin, C. Miao, H. Du, B. Li, Q.-H. Yang, Z. Lin, T. S. Zhao and F. Kang, *Nano Energy*, 2016, **22**, 278-289.
64. X. Zhu, W. Jiang, S. Zhao, R. Huang, M. Ling, C. Liang and L. Wang, *Nano Energy*, 2022, **96**, 107093.
65. C. Shi, G. V. Alexander, J. O'Neill, K. Duncan, G. Godbey and E. D. Wachsman, *ACS Energy Letters*, 2023, **8**, 1803-1810.
66. N. W. Utomo, Y. Deng, Q. Zhao, X. Liu and L. A. Archer, *Advanced Materials*, 2022, **34**, 2110333.
67. Y. Liu, D. Yang, W. Yan, Q. Huang, Y. Zhu, L. Fu and Y. Wu, *iScience*, 2019, **19**, 316-325.
68. C. Li, Q. Zhang, J. Sheng, B. Chen, R. Gao, Z. Piao, X. Zhong, Z. Han, Y. Zhu, J. Wang, G. Zhou and H.-M. Cheng, *Energy & Environmental Science*, 2022, **15**, 4289-4300.
69. S. Murugan, S. V. Klostermann, P. Schützendübe, G. Richter, J. Kästner and M. R. Buchmeiser, *Adv. Funct. Mater.*, 2022, **32**, 2201191.
70. J. Zhang, J. Chou, X.-X. Luo, Y.-M. Yang, M.-Y. Yan, D. Jia, C.-H. Zhang, Y.-H. Wang, W.-P. Wang, S.-J. Tan, J.-C. Guo, Y. Zhao, F. Wang, S. Xin, L.-J. Wan and Y.-G. Guo, *Angew. Chem. Int. Ed. Engl.*, 2023, **n/a**, e202316087.